



**OPTIMAL SYSTEM-MIX OF FLEXIBILITY  
SOLUTIONS FOR EUROPEAN ELECTRICITY**

# Quantification of multi-service synergy

**D3.4**



**Contact: [www.osmose-h2020.eu](http://www.osmose-h2020.eu)**



The project has received funding from the European Union's Horizon 2020 research and innovation programme under grant agreement No 773406

## Document properties

### Project information

Programme	Optimal System-Mix Of Flexibility Solutions For European Electricity
Project Acronym	OSMOSE
Grant agreement	773406
Number of the Deliverable	D3.4
WP/Task related	3

### Document information

Document Name	<b>Quantification of multi-service synergy</b>
Date of Delivery	
Status and version	V1
Number of Pages	45

### Responsible

Responsible	Yihui Zuo (yihui.zuo@epfl.ch)
Authors	Yihui Zuo, Francesco Gerini, Antonio Zecchino, Zhao Yuan, Rachid Cherkaoui, Mario Paolone (Distributed Electrical Systems Laboratory, EPFL, Lausanne, Switzerland), Carmen Cardozo, Thibault Prevost, Yannick Vernay, Guillaume Denis (RTE, La Défense, France), Markel Zubiaga Lazkano, Juan Jose Valera (Ingeteam R&D, Bilbao, Spain)
Reviewers	Alberto Escalera, Luca Orrù (Terna, Italy)
Approver	Nathalie Grisey (RTE, France)

### Dissemination level

Type (distribution level)	<b>PU Public</b>
	<del>GO — full consortium, Confidential, only for members of the consortium (including the Commission Services)</del>
	<del>GO — some partners, Confidential, only for some partners (list of partners to be defined)</del>

### Review history

Version	Date	Reviewer	Comment
V0	February 28, 2022	RTE	Draft for internal WP 3 review
V1	March 7, 2022	Steering Committee	For review

## Table of content

<b>List of Acronyms</b>	<b>7</b>
<b>1. Introduction</b>	<b>8</b>
1.1. Motivations . . . . .	8
1.2. Recall of WP3 objectives and outline of this deliverable . . . . .	9
<b>2. Optimal provision of concurrent primary frequency and local voltage control from a BESS considering variable capability curves</b>	<b>11</b>
2.1. Proposed methodology . . . . .	11
2.2. Utility-scale BESS capability curves and assessment of its equivalent circuit model . . .	16
2.3. Experimental investigation . . . . .	20
<b>3. Optimal grid-forming control of a battery energy storage system providing multiple services</b>	<b>26</b>
3.1. Problem statement . . . . .	26
3.2. Multiple-services control framework for a BESS operating in grid-forming mode . . . .	27
3.2.1. Day-Ahead Stage . . . . .	27
3.2.2. Intra-day Stage . . . . .	29
3.2.3. Real-Time Control Stage . . . . .	32
3.3. Experimental validation . . . . .	34
3.3.1. Experimental Setup . . . . .	34
3.3.2. Experimental Validation . . . . .	34
<b>4. Conclusions</b>	<b>40</b>
<b>A. Forecasting Tools</b>	<b>44</b>

## List of Figures

2.1. BESS converter PQ capability curves as function of $v_t^{AC}$ and $v_t^{DC}$ . . . . .	12
2.2. Three time constant TTC model. . . . .	13
2.3. Reference BESS scheme for the AC voltage prediction. . . . .	14
2.4. Block diagram of the proposed real-time controller. . . . .	15
2.5. PRBS active power reference and measured SOC, $v^{DC}$ and $i^{DC}$ for the SOC range of 34-66% in case of 7 strings in operation. . . . .	18
2.6. 1 month historical data of frequency and phase-to-phase voltage at the BESS PCC at 21 kV, acquired via PMUs installed at the EPFL MV network. The dashed lines represent the limits of $\mu_f \pm 3.3\sigma_f$ and $\mu_V \pm 1\sigma_V$ for frequency and voltage measurements, respectively. . . . .	19
2.7. <i>Scenario#1</i> Results. (a): FCR; (b): local voltage control. . . . .	21
2.8. <i>Scenario#2</i> Results. (a): FCR; (b): local voltage control. . . . .	21
2.9. <i>Scenario#3</i> Results. (a): FCR; (b): local voltage control; (c): PQ set-points before and after the proposed optimization algorithm. . . . .	23
2.10. <i>Scenario#4</i> Results. (a): FCR; (b): local voltage control; (c): PQ set-points before and after the proposed optimization algorithm. . . . .	24
3.1. Control Scheme for grid forming control . . . . .	27
3.2. Topology of the feeder for the problem statement . . . . .	28
3.3. Timeline for the MPC problem . . . . .	30
3.4. Input and output of the day-ahead problem. (a) shows 10 demand generated scenarios, and their relative upper and lower bound. (b) shows the upper and lower bound for the PV production. (c) combines load and PV to show the prosumption scenario, input of the day ahead problem. (d) and (e) show the power and energy budget allocated to perform the different services. . . . .	36
3.5. Experimental results for the 24-hour test. (a) compares the dispatch plan (in black) with: the measured power at the PCC (shaded gray), the prosumption of the feeder (in dashed red), the BESS power flow (in shaded red) and the average power required for each 5-minutes window for the provision of FCR service by the BESS. (b) shows the grid-frequency and its 5-minutes mean. The SOE of the battery during the test is visible in (c). . . . .	37
3.6. Cumulative Density Function of rRoCoF. . . . .	39

## List of Tables

2.1. Specifications of the employed utility-scale BESS . . . . .	16
2.2. Fitted Functions of the Converter PQ Capability Curves . . . . .	17
2.3. Estimated BESS Parameters for 7 strings for different SOC ranges . . . . .	18
2.4. Calculated $\alpha_0$ and $\beta_0$ for different shrink factors $C_{shrink}$ . . . . .	19
2.5. Calculated $\alpha_0$ and $\beta_0$ for different shrink factors $C_{shrink}$ . . . . .	20
2.6. Expected and delivered energy for FCR with and without the proposed optimization algorithm . . . . .	23
3.1. Tracking error statistics (in kW) . . . . .	35

## Executive Summary

Thanks to their fast ramping rate and bidirectional power flow, grid-connected Battery Energy Storage Systems (BESS) are advocated as a promising technology for mitigating the variability of stochastic renewable generation but also as a potential remedy for power grid frequency regulation. In this respect, the development of control strategies able to couple multiple services allows for a better exploitation of the BESS associated to stochastic resources. This deliverable assesses the performance of proposed multi-service control frameworks for BESS via the results of experimental demonstration activities. The demonstrations are carried out on the EPFL (*École Polytechnique Fédérale de Lausanne*) site that allows for the validation of the grid-forming controller and other grid services on real industry-grade hardware connected to realistic power distribution grids. Specifically, the demonstration activities are achieved with a 720kVA/560kWh Lithium Titanate Oxide BESS, connected to a 20 kV feeder of the EPFL Campus, whose surrounding grid is meshed with proprietary *Phasor Measurement Units* (PMUs) of high accuracy. The performance of the following two multi-service controls are investigated:

- A BESS control framework for optimal provision of concurrent primary frequency and local voltage control considering dynamic converter capability curves;
- A joint control and scheduling framework for *grid-forming* (GFM) converter-interfaced BESSs providing multiple services (i.e., feeder dispatchability, frequency, and voltage regulation).

The first control framework is proposed for the concurrent provision of power system frequency and local voltage control based on the real-time solution of an optimization problem that maximizes the contribution to grid support. The proposed method considers the variability of the feasibility PQ region of the BESS power converter as a function of both the AC grid and internal BESS conditions. A set of experimental tests demonstrate the importance of accurately modelling the employed hardware in order to enable an optimal grid service provision even under non-nominal BESS conditions (e.g., reduced the available number of strings) as well as under commercial hardware embedded technical limitations (e.g., variable capability curves of the power converter).

The second control framework is developed for GFM converter-interfaced BESS, tackling the optimal provision of multiple services (i.e., feeder dispatchability, frequency and voltage regulation) to maximize the battery exploitation in the presence of uncertainties due to stochastic demand, distributed generation, and grid frequency. The proposed framework is experimentally validated by using the 720kVA/560 kWh BESS to dispatch the operation of a 20 kV distribution feeder hosting both conventional consumption and distributed *Photo-Voltaic* (PV) generation. A 24-hour long experiment proves the good performance of the proposed control algorithm in terms of dispatch tracking. The proposed key performance indicator quantitatively shows that the provision of dispatchability service by the GFM converter does not affect its frequency regulation performance and confirms the positive effects of grid-forming converters with respect to the grid-following ones in the control of the local frequency.

## List of Acronyms

<b>AS</b>	.....	Ancillary Service
<b>BESS</b>	.....	Battery Energy Storage System
<b>FCR</b>	.....	Frequency Containment Reserve
<b>GFM</b>	.....	Grid-forming
<b>GFL</b>	.....	Grid-following
<b>KPI</b>	.....	Key Performance Indicator
<b>PFC</b>	.....	Primary Frequency Control
<b>PMU</b>	.....	Phasor Measurement Unit
<b>PCC</b>	.....	Point Of Common Coupling
<b>RoCoF</b>	.....	Rate of Change of Frequency
<b>rRoCoF</b>	.....	relative Rate of Change of Frequency
<b>SOC</b>	.....	State of Charge
<b>TTC</b>	.....	Three-time Constant
<b>VSC</b>	.....	Voltage Source Converter

## 1. Introduction

### 1.1. Motivations

Given the progressive displacement of conventional generation plants in favor of stochastic renewable-based generation units, it is increasingly needed for Transmission System Operators (TSOs) to restore an adequate regulating power capability to assure reliable operation of interconnected power systems. In this context, network operators are motivated to set demanding requirements on the dispatchability of connected resources and to incorporate assets with high ramping capability to maintain frequency containment performance [1, 2]. An emerging concept to tackle the challenge of dispatchability of power distribution systems hosting stochastic power generation is to exploit utility-scale Battery Energy Storage Systems (BESSs). Besides, as extensively demonstrated in the literature, one of the most popular power system services achieved by BESS is frequency regulation [3]. Moreover, since power converters are normally able to operate on the four quadrants of their PQ capability curve, they are also capable of exchanging reactive power concurrently with the active power. In this respect, control approaches of BESS providing multiple ancillary services to the power system are of high interest to fully take advantage of BESSs investments. When a portion of the BESS energy capacity remains unexploited by the deployment of its main service, it could be allocated to other services, to be deployed simultaneously.

The state-of-the-art has presented optimal solution for ancillary services provision [4, 5]. In particular, [4] proposes to solve an optimization problem that allocates the battery power and energy budgets to different services in order to maximize battery exploitation. Nevertheless, the dispatch tracking problem is oversimplified and does not ensure the BESS operation to be within the physical limits. Indeed, the existing scientific literature typically assumes that the PQ capability curve of the BESS converter to be unique and independent from the battery State-Of-Charge (SOC) and the AC grid voltage conditions [6, 7]. However, the actual physical constraint of the BESS power converter has a non-unique PQ region of feasibility. In this respect, it is crucial to consider the working conditions of the AC utility grid and the battery DC voltage to select the suitable converter capability curve, hence optimizing the provision of oriented services. On the other hand, [5] tackles the problem of dispatching the operation of a cluster of stochastic prosumers through a two-stage process, which consists of a day-ahead dispatch plan determined by the data-driven forecasting and a real-time operation tracking the dispatch plan via adjusting the real power injections of the BESS with a *Model Predictive Control* (MPC).

Despite the efforts, all the proposed solutions rely on *grid-following* (GFL) control strategies, rarely exploring the possibility of controlling the BESS converter in *grid-forming* (GFM) mode. Recent studies have proved GFM control strategies to outperform GFL in terms of frequency regulation performance in low-inertia power grids [8]. Furthermore, the impact of GFM converters on the dynamics of a reduced-inertia grids has been investigated in [9], which quantitatively proved the good performance of GFM units in limiting the frequency deviation and in damping the frequency oscillations in case of large power system contingencies. Nevertheless, the existing scientific literature lacks of studies assessing the performance of GFM units in supporting the frequency containment process of large interconnected power grids. Moreover, to the best of the authors' knowledge, GFM units have never been proved able to provide services such as feeder dispatchability. In fact, studies on the GFM units synchronizing with AC grids are mostly limited to ancillary services provision and their validations is based on either simulation [8–10] or to experiments on ideal slack buses with emulated voltage [11, 12].

With respect to the existing literature discussed in this section, the contributions of this deliverable are the following.

- 
- Propose a method that accounts for the variability of the feasibility PQ region of the BESS power converter as function of both the AC grid and internal BESS conditions.
  - Develop a control framework for concurrent provision of power system frequency and local voltage control based on the real-time solution of an optimization problem to maximize the contribution to grid support that the BESS can provide for given actual and predicted operating conditions.
  - Propose the development of a control framework for GFM converter-interfaced BESS, tackling the optimal provision of multiple services and its experimental validation. The framework consists of three stages: a day-ahead scheduling stage, an intra-day stage and a real-time stage. The first two stages are not affected by whether the BESS is operated in GFM or GFL mode. What differentiates the GFM and GFL mode is the third stage where the power set-point originated by the dispatch tracking is converted into a feasible frequency/voltage set-point for the grid-forming converter by means of a convex optimisation problem accounting for the capability curve of the power converter.
  - Assess the performance of the GFM-controlled BESS providing simultaneously dispatching tracking and frequency containment reserve (FCR) provision. In particular, the frequency regulation performance of the GFM-controlled BESS is evaluated and compared with the case of GFM only providing FCR and with the GFL case.

It is worth mentioning that the demonstration part of this work relies on experiments performed on specific hardware (experimental facility in EPFL). Therefore, the developed control techniques must fit in the framework of this existing hardware that has limited exchange possibility. In other words, the grid-forming control is not developed for the purpose of this experiment as it was possible in the RTE-Ingteam Demo, but it consists of a commercial solution. This drives several limitations and workarounds on the formulation of the problem and optimization. Nevertheless, the results show that the behavior is acceptable (see 5.4 of [13]). Here, voltage ( $V_{ref}$ ) and frequency ( $F_{ref}$ ) references are the inputs of the grid-forming controller and updated using Modbus protocol and external controls (see 6.1 of [13]). Therefore, it is required to convert the active and reactive power set-point into voltage and frequency references to feed the GFM converter. Another noteworthy limitation of the existing hardware is that without the proposed optimal controller, an unfeasible power set-point sent to the BESS controller could trip the BESS converter or result into the actuation of a null power set-point for safety reasons. For this reason, we propose a method to retrieve the set-point back in the feasible region in case the original computed values are too high, thus assuring the continuity of the delivery of both grid services.

## 1.2. Recall of WP3 objectives and outline of this deliverable

In this work, we assess the performance of the multi-service control algorithms based on the demonstration results on an existing MW-scale BESS connected to one of the medium voltage feeders supplying the EPFL campus. The demonstration includes a dedicated PMU-based infrastructure for metering and data logging of the EPFL medium voltage grid in addition to the proposed multi-service control algorithms. This deliverable quantitatively evaluates the synergy effect brought by the provision of several services with only one converter and it is structured as follows:

Chapter 2 proposes a control framework for the concurrent provision of power system frequency and local voltage control based on the real-time solution of an optimization problem that maximizes the contribution to grid support. The proposed method considers the variability of the feasibility PQ region of the BESS power converter as a function of both the AC grid and internal BESS conditions. A set of experimental tests validate the proposed concepts and show the effectiveness of the employed control framework on a commercial utility-scale 720 kVA/560 kWh BESS.

---

Chapter 3 discusses a control framework for GFM converter-interfaced BESS, tackling the optimal provision of multiple services. The control framework for the simultaneous provision of feeder dispatchability, FCR, and voltage regulation aims to maximize the battery exploitation in the presence of uncertainties due to stochastic demand, distributed generation, and grid frequency. Similarly to the results shown in Chapter 2, the experimental validation of the proposed framework is conducted by using a 560 kWh BESS interfaced with a 720 kVA GFM-controlled converter to dispatch the operation of a 20 kV distribution feeder hosting both conventional consumption and distributed Photo-Voltaic (PV) generation. The performance of the GFM-controlled BESS providing simultaneously dispatching tracking, FCR and inertial response is assessed. In particular, the frequency regulation performance of the GFM-controlled BESS is evaluated and compared with the case of GFL- and GFM-controlled BESS providing uniquely the FCR service, without any dispatch tracking. Finally, Chapter 4 draws the conclusion.

## 2. Optimal provision of concurrent primary frequency and local voltage control from a BESS considering variable capability curves

In this Chapter, a control method for BESSs to provide concurrent Frequency Containment Reserve (FCR) and local voltage regulation services is proposed. The actual variable active and reactive power capability of the converter, along with the state-of-charge of the BESS, are jointly considered by an optimal operating point calculation process within the real-time operation of the BESS. The controller optimizes the provision of grid services considering the measured grid and battery statuses and predicting the battery DC voltage as a function of the current trajectory using a Three-Time-Constant model (TTC). A computationally-efficient algorithm is proposed to solve the formulated optimal control problem. Experimental tests validate the proposed concepts and show the effectiveness of the employed control framework on a commercial utility-scale 720 kVA/560 kWh BESS.

NOTE: *The content of this Section has been published within the framework of the Osmose project: Antonio Zecchino, Zhao Yuan, Fabrizio Sossan, Rachid Cherkaoui, Mario Paolone, "Optimal provision of concurrent primary frequency and local voltage control from a BESS considering variable capability curves: Modelling and experimental assessment", Electric Power Systems Research, Vol. 190, 2021, 106643, ISSN 0378-7796, <https://doi.org/10.1016/j.epsr.2020.106643>.*

### 2.1. Proposed methodology

The BESS converter is controlled to provide frequency containment reserve and local voltage regulation adjusting the active and reactive power set-points, respectively. The initial power set-points are achieved via droop logics:

$$P_{0,t}^{AC} = \alpha_0 \Delta f_t; Q_{0,t}^{AC} = \beta_0 \Delta v_t^{AC}, \quad (2.1)$$

where  $t \in T$  is the discrete index of time,  $P_{0,t}^{AC}, Q_{0,t}^{AC}$  are the initial active and reactive power set-points that the BESS will set for given grid frequency and AC voltage magnitude deviations from their nominal values ( $\Delta f_t, \Delta v_t^{AC}$ ), according to the initial droop coefficients  $\alpha_0, \beta_0$ . These active and reactive power set-points will be adjusted when considering the converter capability curves, as will be described later in this Chapter.

To maximize the frequency and voltage regulation performance, the initial droop coefficients  $\alpha_0, \beta_0$  can be set as:

$$\alpha_0 = \frac{P^{max}}{\Delta^{max} f_t}; \beta_0 = \frac{Q^{max}}{\Delta^{max} v_t^{AC}}, \quad (2.2)$$

where  $P^{max}$  and  $Q^{max}$  are the maximum active and reactive power that the BESS can exchange, as specified by the BESS technical specifications. Historical measurements can be used to determine the maximum frequency and voltage deviation  $\Delta^{max} f_t, \Delta^{max} v_t^{AC}$ , as shown in Section III. During real-time operations, the employed  $\alpha_t, \beta_t$  are adjusted by relying on BESS status (available storage capacity and SOC) and solving an optimal power set-points calculation problem Eq. (2.14).

Commonly, in the current literature the converter capability is considered to be constantly expressed as  $(P_t^{AC})^2 + (Q_t^{AC})^2 \leq (S^{AC})^2$ , where  $P_t^{AC}, Q_t^{AC}$ , and  $S^{AC}$  are the converter output active, reactive and maximum apparent power of the grid converter, respectively. This assumption, however, does not hold in practice. In this work, the realistic feasible operation region identified by the PQ converter

capability curves  $h$  in Fig. 2.1, are considered as:

$$h(P_t^{AC}, Q_t^{AC}, v_t^{DC}, v_t^{AC}, SOC_t) \leq 0 \quad (2.3)$$

being  $v_t^{DC}$  the voltage of the BESS DC bus and  $v_t^{AC}$  the module of the positive sequence component of the phase-to-phase voltages at the AC side. Notably, the capability curves  $h$  are specific for the employed hardware, but similar dependencies are expected in all kinds of utility-scale BESS converters. More detailed information about the PQ curves considered in this study are included in Section III.

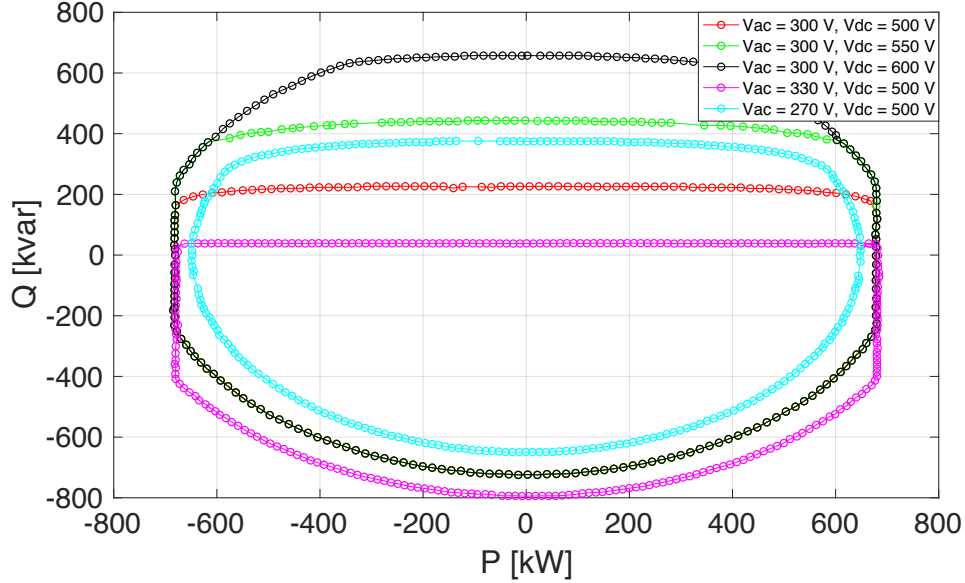


**Figure 2.1:** BESS converter PQ capability curves as function of  $v_t^{AC}$  and  $v_t^{DC}$ .

The  $v_t^{DC}$  voltage needed for the selection of the capability curve is estimated via the Three-Time-Constant (TTC) model shown in Fig. 2.2, whose parameters are derived by dedicated model identification tests. Since the BESS has to be controlled at a sub-second level, we estimate the BESS status based on the TTC model state equations:

$$C_1 \frac{dv_{C1}}{dt} + \frac{v_{C1}}{R_1} = \frac{v_s}{R_s} \quad (2.4)$$

$$C_2 \frac{dv_{C2}}{dt} + \frac{v_{C2}}{R_2} = \frac{v_s}{R_s} \quad (2.5)$$

$$C_3 \frac{dv_{C3}}{dt} + \frac{v_{C3}}{R_3} = \frac{v_s}{R_s} \quad (2.6)$$

$$v_s + v_{C1} + v_{C2} + v_{C3} = E - v_t^{DC}, \quad (2.7)$$

where  $\mathbf{v}_c = [v_{C1}; v_{C2}; v_{C3}]$  are the TTC state voltage variables that are updated by solving Eqs. (2.4) to (2.7) in each control loop. At each time step, the initial value of the state variables can be estimated via the use of dedicated state observers as proposed in [14]. The model Eqs. (2.4) to (2.7) is discretized at a 1s resolution in this Chapter. The TTC model capacitance parameters  $C_1, C_2, C_3$  and resistance parameters  $R_s, R_1, R_2, R_3$  are identified by generating active power Pseudo Random Binary Signals (PRBS) and then by measuring the corresponding current dynamics. This process is explained in Section III. The voltage source  $E$  is the open circuit voltage of the battery, which depends on the SOC as shown in Eq. (2.8).  $E$  is modelled as a linear function of the battery SOC, where the

parameters  $a$  and  $b$  are identified within the TTC model identification process.

$$E(SOC_t) = a + b \cdot SOC_t \quad (2.8)$$

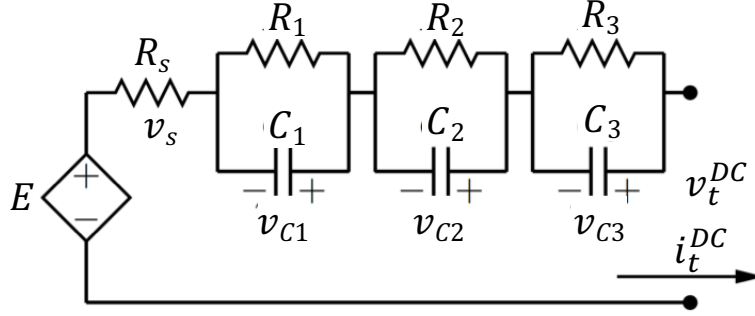


**Figure 2.2:** Three time constant TTC model.

After updating  $\mathbf{v}_c = [v_{C1}; v_{C2}; v_{C3}]$ , considering  $v_s = \frac{P_t^{DC}}{v_t^{DC}} R_s$ , Eq. (2.7) is equivalent to:

$$(v_t^{DC})^2 + (\mathbf{1}^T \mathbf{v}_c - E)v_t^{DC} + P_t^{DC} R_s = 0, \quad (2.9)$$

where  $\mathbf{1}^T = [1, 1, 1]$ . Solving constraint Eq. (2.3) jointly with Eq. (2.9) gives feasible power set-points  $P_t^{AC}, Q_t^{AC}$  satisfying the evolving capability curves during the control loop.

Given the initial state-of-charge  $SOC_0$ , its value at each discrete time control iteration,  $SOC_t$ , can be expressed as:

$$\begin{aligned} SOC_t &= SOC_{t-1} + \frac{\int_{t-1}^t i_t^{DC} dt}{C^{rated}} \\ &\approx SOC_{t-1} + \frac{P_t^{DC}}{v_t^{DC} C^{rated}} \Delta t, \end{aligned} \quad (2.10)$$

where  $C^{rated}$  is the rated storage capacity of the battery in Ampere-hour and  $i^{DC} \approx \frac{P_t^{DC}}{v_t^{DC}}$  is the charging or discharging DC current. The active power at the DC bus  $P_t^{DC}$  is related the active power at the AC side of the converter as:

$$P_t^{DC} = \begin{cases} \eta P_t^{AC}, & \forall P_t^{AC} < 0 \\ \frac{P_t^{AC}}{\eta}, & \forall P_t^{AC} \geq 0 \end{cases}, \quad (2.11)$$

where  $\eta$  ( $\approx 97\%$ ) is the efficiency of converter.  $P_t^{AC} < 0$  means charging of the BESS and  $P_t^{AC} \geq 0$  means discharging. The state-of-charge  $SOC_t$  should be always kept in the secure limits during all the operational periods  $t \in T$ :

$$SOC^{min} \leq SOC_t \leq SOC^{max} \quad (2.12)$$

The magnitude of the direct sequence component  $v_t^{AC}$  of the phase-to-phase voltages needed for the selection of the converter capability curve is estimated via the Thévenin equivalent circuit of the AC grid. As shown by Eq. (2.13), the estimation considers the direct sequence component  $v_t^{AC,m}$  of the measured phase-to-phase voltages and the expected voltage drop due to the three-phase complex power  $S_{0,t}^{AC}$  exchanged by the BESS over the grid equivalent impedance  $\mathbf{Z}_{eq}$ .  $\mathbf{Z}_{eq}$

can be approximated as the BESS step-up transformer reactance  $jX_T$ . Since, as shown in Fig. 2.3, measurements are acquired at the primary side of the BESS step-up transformer whereas the estimation is done for the voltage at the secondary side, the voltage  $\mathbf{v}_t^{AC,m}$  in Eq. (2.13) is referred to the secondary side as  $\mathbf{v}_t^{AC,m} = \mathbf{v}_{MV,t}^{AC,m} \frac{1}{n}$ , being  $n$  the transformer ratio.

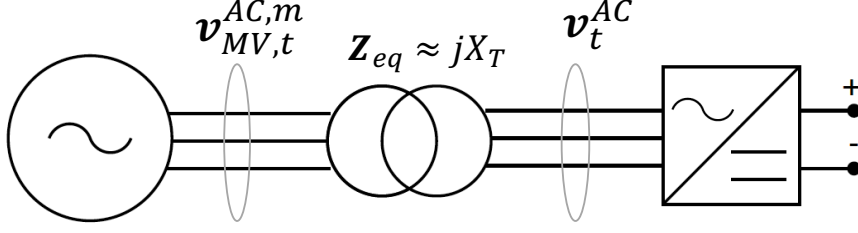


**Figure 2.3:** Reference BESS scheme for the AC voltage prediction.

$$\mathbf{v}_t^{AC} = \mathbf{v}_t^{AC,m} + \mathbf{Z}_{eq} \text{conj} \left( \frac{\mathbf{S}_{0,t}^{AC}}{\sqrt{3} \mathbf{v}_t^{AC,m}} \right)$$

$$v_t^{AC} \approx \sqrt{(v_t^{AC,m})^2 + X_T^2 \frac{(P_{0,t}^{AC})^2 + (Q_{0,t}^{AC})^2}{3(v_t^{AC,m})^2}} \quad (2.13)$$

The optimal active and reactive power set-points are given by solving the following optimization problem:

$$\begin{aligned} & \text{Minimize } \lambda_P (P_t^{AC} - P_{0,t}^{AC})^2 + \lambda_Q (Q_t^{AC} - Q_{0,t}^{AC})^2 \\ & \text{subject to } (2.1) - (2.3), (2.9) - (2.13) \end{aligned} \quad (2.14)$$

Where  $\lambda_P$  and  $\lambda_Q$  are weight coefficients used by the modeler to prioritize the provision of active or reactive power, i.e., to prioritize one grid service over the other. In the case of equal priority for frequency and voltage control, the weight of 1 is assigned to both coefficients, meaning that the optimal power set-points  $P_t^{AC}, Q_t^{AC}$  are the closest to the initial power set-points  $P_{0,t}^{AC}, Q_{0,t}^{AC}$  inside the feasible operational region of the BESS defined by Eqs. (2.1) to (2.3) and Eqs. (2.9) to (2.12). After finding the optimal power set-points  $P_t^{*AC}, Q_t^{*AC}$ , the optimal droop parameters  $\alpha_t^*, \beta_t^*$  are defined as:

$$\alpha_t^* = \frac{P^{*AC}}{\Delta f_t}; \quad \beta_t^* = \frac{Q^{*AC}}{\Delta v_t^{AC}} \quad (2.15)$$

This optimization problem is nonconvex due to the nonconvex constraints Eq. (2.9), Eq. (2.10) and Eq. (2.11). To efficiently find a local optimal solution, constraint Eq. (2.9) is firstly convexified to:

$$(v_t^{DC})^2 + (\mathbf{1}^T \mathbf{v}_c - E) v_t^{DC} + P_t^{DC} R_s \leq 0 \quad (2.16)$$

This relaxation shows better computational efficiency in real-time control experiments. Then, to find the optimal power set-points, we propose the computationally-efficient solution algorithm shown in Algorithm 1, where  $V_i^{DC} \in \{(500, 550], (550, 600], (600, 800]\}$  is  $i$ -th set of the DC voltage range<sup>1</sup> and where  $V_j^{AC} \in \{(270, 300], (300, 330], (330, +Inf)\}$  is  $j$ -th set of the AC voltage range<sup>2</sup>. Algorithm 1 works by firstly assuming the ranges that could include the DC voltage  $v_t^{DC}$  and the AC voltage

<sup>1</sup>The DC voltage range  $V^{DC}$  lies in the interval  $[500 \text{ V}, 800 \text{ V}]$ .

<sup>2</sup>The AC voltage range lies in the interval  $[270 \text{ V}, +Inf]$ .

$v_t^{AC}$  solutions. Then, one capability curve is selected based on the assumed DC voltage and the predicted AC voltage. If the calculated  $v_t^{DC}$  and  $v_t^{AC}$  are consistent with the initial assumed DC and AC voltage ranges  $V_i^{DC}$  and  $V_j^{AC}$ , the algorithm converges. Otherwise, the assumption of the DC and AC voltage ranges is changed and another capability curve is selected until a consistent solution is found.

---

**Algorithm 1:** Optimization Solution Algorithm

---

**Result:** Optimal Power Set-Points  $P_t^{AC}, Q_t^{AC}$

Initialization  $P_0^{AC}, Q_0^{AC}, i = 1, j = 1;$

```

while  $v_t^{DC} \notin V_i^{DC}$  and  $i < i^{max}$  do
  Assume  $v_t^{DC} \in V_i^{DC};$ 
  while  $v_t^{AC} \notin V_j^{AC}$  and  $j < j^{max}$  do
    Assume  $v_t^{AC} \in V_j^{AC};$ 
    Select one capability curve:  $h(P_t^{AC}, Q_t^{AC}, v_t^{DC}, v_t^{AC}, SOC_t);$ 
    if  $P_0^{AC} < 0$  then
      |  $P_t^{DC} = \eta P_t^{AC};$ 
    else
      |  $P_t^{DC} = \frac{P_t^{AC}}{\eta};$ 
    end
    Solve the Optimization Problem;
     $j = j + 1;$ 
  end
   $i = i + 1;$ 
end

```

---

The block diagram of the proposed controller during one time step is illustrated in Fig. 2.4.

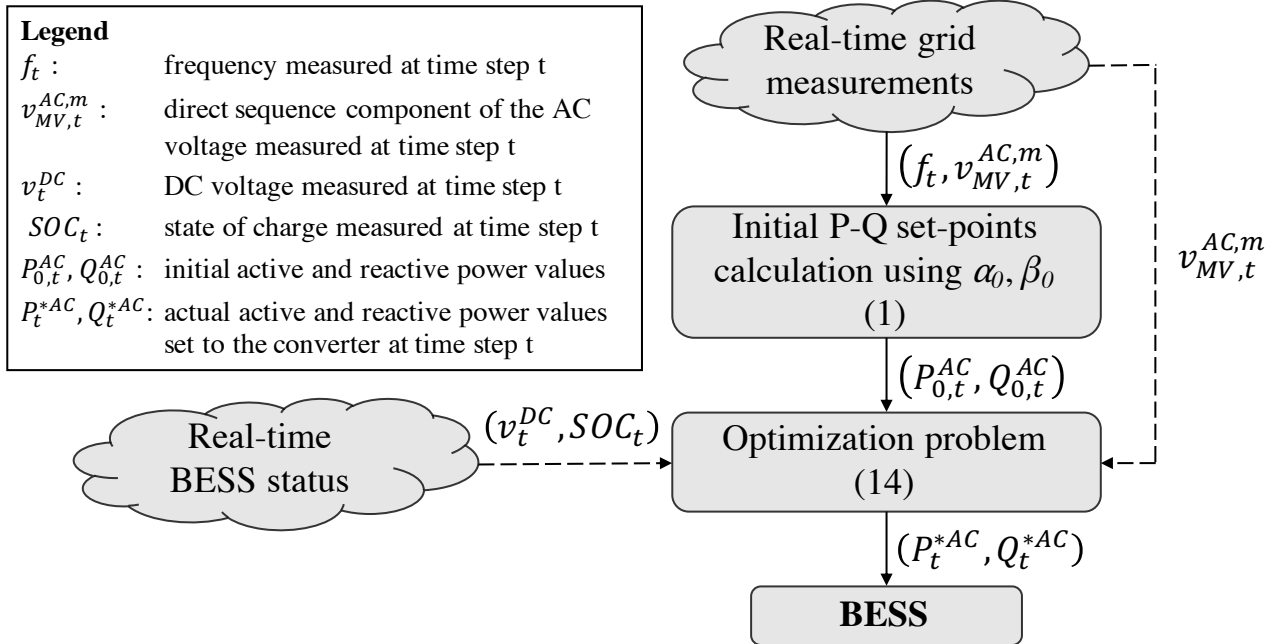


**Figure 2.4:** Block diagram of the proposed real-time controller.

## 2.2. Utility-scale BESS capability curves and assessment of its equivalent circuit model

The experimental setup used for the validation of the control framework consists in an utility-scale BESS installed at the EPFL campus in Lausanne, Switzerland. The system is based on a 720 kVA/560 kWh Lithium-Titanate-Oxide (LTO) battery, utilized for a number of power grid support experimental activities [15]. The BESS is equipped with a 720 kVA 4-quadrants converter, which can be controlled via *Modbus TCP* with a refresh rate up to 50 ms. The BESS is connected to one of the feeders of the EPFL campus medium voltage (MV) grid via a 630 kVA 3-phase 0.3/21 kV step-up transformer. The parameters of the main components of the employed BESS are reported in Table 2.1. The selected MV feeder presents all the peculiarities of modern active distribution grids: the lines are relatively short, the load demand is largely variable during the day (office buildings with 300 kW of max load), and a substantial amount of rooftop PV units is connected (for a total of 95 kWp). Such characteristics make the testbed suitable for investigations not only on system frequency regulation, but also on local voltage control solutions such as the one proposed in this work.

**Table 2.1:** Specifications of the employed utility-scale BESS

Parameter	Value
Energy Capacity	560 kWh
Maximum Power	720 kVA
Nominal Active Power	640 kW
Rated AC grid voltage	0.3 kV, three-phase
Maximum AC current	1385 A
AC current distortion (THD)	3%
Nominal DC voltage	750 V
DC voltage range	500-890 V
Inverter efficiency	$\geq 97\%$
Transformer rated power	630 kVA
Transformer high voltage	3 x 21 kV
Transformer low voltage	3 x 0.3 kV
Transformer short-circuit voltage	6.28%
Transformer group	Dd0

As known, the peculiarity of BESSs is their modular structure. For the specific commercial MW-class BESS under analysis, 3 series of 20 cell elements are connected in parallel to compose a BESS module, 15 modules in series compose one string, and finally 9 strings connected in parallel guarantee the desired BESS energy storage and power capacity. The main advantage of such modular structure is the absence of a single point of failure at all level. In fact, the system can be operated even if one or more strings are not in operation. In this respect, in the analysis proposed in this work a configuration with reduced number of strings is considered. Specifically, 7 strings out of 9 are utilized, meaning that the BESS available storage capacity is 7/9 of the total value, i.e., 435 kWh. One has to note that the reduced number of usable strings should be considered also in the setting of the maximum power exchange capability, being the strings connected in parallel. This is done to prevent string over-currents and over-temperatures, without jeopardizing the cycle aging process of the cells. In this respect, at the implementation stage of the controller, the constraints of the power converter PQ capability curves presented in Fig. 2.1 have been shrank by the factor  $C_{shrink}$ , which in this case is 7/9.

As shown in Fig. 2.1, the region of feasible operating points of the power converter depends on the grid AC voltage and on the DC battery voltage in a non-linear way. In fact, for increasing battery DC

voltages only the maximum positive Q value is increasing. The curve is shifted down vertically for AC voltages higher than the nominal value, meaning that both the maximum positive Q is decreased, whereas the maximum negative Q is increased. A different pattern is present for AC voltages lower than the nominal value: the limit values are shrank both for the active and the reactive part of the apparent power set-point in both negative and positive signs. Regarding the implementation of the proposed controller, the dependency of the feasibility region on the grid and battery statuses is considered in a discretized way by selecting two of the five PQ curves and by considering the overlapping area between them. As previously mentioned, this is done in accordance with the respective factor  $C_{shrink}$ . The capability curves of the employed power converter are fitted using datasheet information from the manufacturer and, then, scaled proportionally to the available BESS capacity. The fitted capability curves consist of a series of linear and quadratic functions, which are reported in Table 2.2.

**Table 2.2:** Fitted Functions of the Converter PQ Capability Curves

$v^{DC}$	$v^{AC}$	Functions
600 V	300 V	$P \geq -681.89$ $P \leq 678.71$ $P^2 + Q^2 \leq 723.03^2, \forall Q \geq 0$ $P^2 + Q^2 \leq 719.19^2, \forall Q < 0$ $Q \leq 659.67 - 8.29^{-18}P - 2.16^{-4}P^2$ $Q \leq 657.1$
550 V	300 V	$P \geq -681.89$ $P \leq 678.71$ $P^2 + Q^2 \leq 723.03^2, \forall Q \geq 0$ $P^2 + Q^2 \leq 717.93^2, \forall Q < 0$ $Q \leq 459.43 - 1.5^{-3}P - 2.12^{-4}P^2$ $Q \leq 439.98$
500 V	300 V	$P \geq -680.62$ $P \leq 682.45$ $P^2 + Q^2 \leq 721.4^2$ $Q \leq 286.64 + 1.4^{-3}P + -2.33^{-4}P^2$ $Q \leq 225.22$
500 V	330 V	$P \geq -679.21$ $P \leq 681.06$ $P^2 + Q^2 \leq 794.34^2$ $Q \leq 38.47$
500 V	270 V	$P^2 + Q^2 \leq 649.5^2$ $Q \leq 382.95 + 1.6^{-3}P - 2.21^{-4}P^2$

A dedicated experimental investigation allowed the estimation of the equivalent TTC circuit parameters via a grey-box modeling-based approach, in line with the analogue estimation activity proposed in [16] for the same BESS in case of full available storage capacity (9 strings). The model identification tests are based on pseudo-random binary sequence (PRBS), i.e., a two levels square wave with on-off periods of normally distributed random durations, capable of exciting a wide range of system dynamics. Fig. 2.5 shows the binary power set-points, the SOC,  $v_{dc}$  and  $i_{dc}$ . Since the TTC model parameters depend on the BESS SOC, the test has been repeated for different SOC ranges. The obtained TTC model parameters are in Table 2.3.

With reference to Eq. (2.2), in order to properly set the initial values of the droop constants  $\alpha_0$  and  $\beta_0$ , the maximum deliverable active and reactive powers  $P^{max}$  and  $Q^{max}$  have been used along with

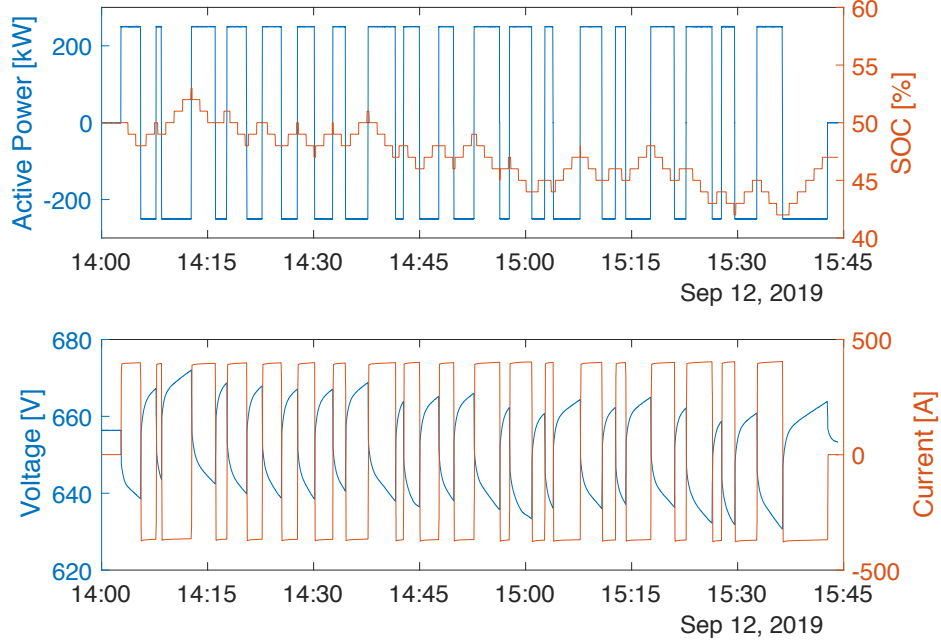


**Figure 2.5:** PRBS active power reference and measured SOC,  $v^{DC}$  and  $i^{DC}$  for the SOC range of 34-66% in case of 7 strings in operation.

**Table 2.3:** Estimated BESS Parameters for 7 strings for different SOC ranges

	SOC=0-33%	SOC=34-66%	SOC=67-100%
$a$	607.2	607.1	590.0
$b$	190.8	113.9	188.9
$R_s$ [ $\Omega$ ]	0.0221	0.0165	0.0155
$R_1$ [ $\Omega$ ]	0.0131	0.0120	0.0109
$C_1$ [ $F$ ]	1511	1844	1917
$R_2$ [ $\Omega$ ]	5.26E-05	2.24E-05	2.55E-04
$C_2$ [ $F$ ]	1.00E+06	1.00E+06	1.00E+06
$R_3$ [ $\Omega$ ]	5.10E-06	6.50E-07	1.55E-05
$C_3$ [ $F$ ]	1.00E+07	1.00E+07	1.00E+07

the calculated maximum deviation of the input variables of the controller, i.e.,  $\Delta^{max} f$  and  $\Delta^{max} v^{AC}$ .

Historical measurements acquired by the synchrophasor network on the EPFL MV network are used for this purpose, whose P-class phasor measurement units (PMUs) allowed the acquisition of data with a timestamp of 20 ms [17]. The values of  $\Delta^{max} f$  and  $\Delta^{max} v^{AC}$  have been obtained by approximating their distribution with normal distribution functions and by considering a relevant multiplication factor for the standard deviations  $\sigma$ . On the one hand, the maximum deviations of  $\pm 3.3\sigma_f$  was considered for the system frequency measurements, meaning that the thresholds  $\mu_f \pm 3.3\sigma_f$  are statistically exceeded only 0.1% of the times, being  $\mu_f$  the average value of the frequency dataset, equal to 50 Hz. This rather strict assumption is motivated by the requirement from the Swiss TSO grid code on the quality of the supply of frequency containment reserve power, which sets a maximum tolerable time of 0.1% of the tender period for which the regulating power cannot be delivered without running into penalties [18]. On the other hand, since less strict requirements regulate the quality of the supply of local voltage control, smaller maximum deviations can be considered: the calculated thresholds for the activation of the maximum reactive power capacity are  $\mu_V \pm 1\sigma_V$ , where  $\mu_V$  is the average value

of the AC phase-to-phase voltage dataset, equal to 21.192 kV. Since the obtained  $\mu_V$  differs from the nominal value of 21 kV, it was decided to consider  $\mu_V$  as reference for the calculation of  $\Delta^{max} v^{AC}$  in Eq. (2.1).

Given the considered historical dataset,  $\Delta^{max} f = \pm 3.3\sigma_f = \pm 58.8$  mHz and  $\Delta^{max} v^{AC} = \pm 1\sigma_V = \pm 0.0672$  kV. The calculated  $\Delta^{max} f$  and  $\Delta^{max} v^{AC}$  enable the computation of the initial droops  $\alpha_0$  and  $\beta_0$  for different BESS configurations considering the number of available strings, i.e., the shrink factors  $C_{shrink}$ , as shown in Table 2.4.

**Table 2.4:** Calculated  $\alpha_0$  and  $\beta_0$  for different shrink factors  $C_{shrink}$

$C_{shrink}$	$\alpha_0$ [kW/Hz]	$\beta_0$ [kvar/V]
1	11575	10.78
8/9	10289	9.58
<b>7/9</b>	<b>9003</b>	<b>8.39</b>
6/9	7717	7.19
5/9	6430	5.99
4/9	5144	4.79
3/9	3858	3.59
2/9	2572	2.40
1/9	1286	1.20

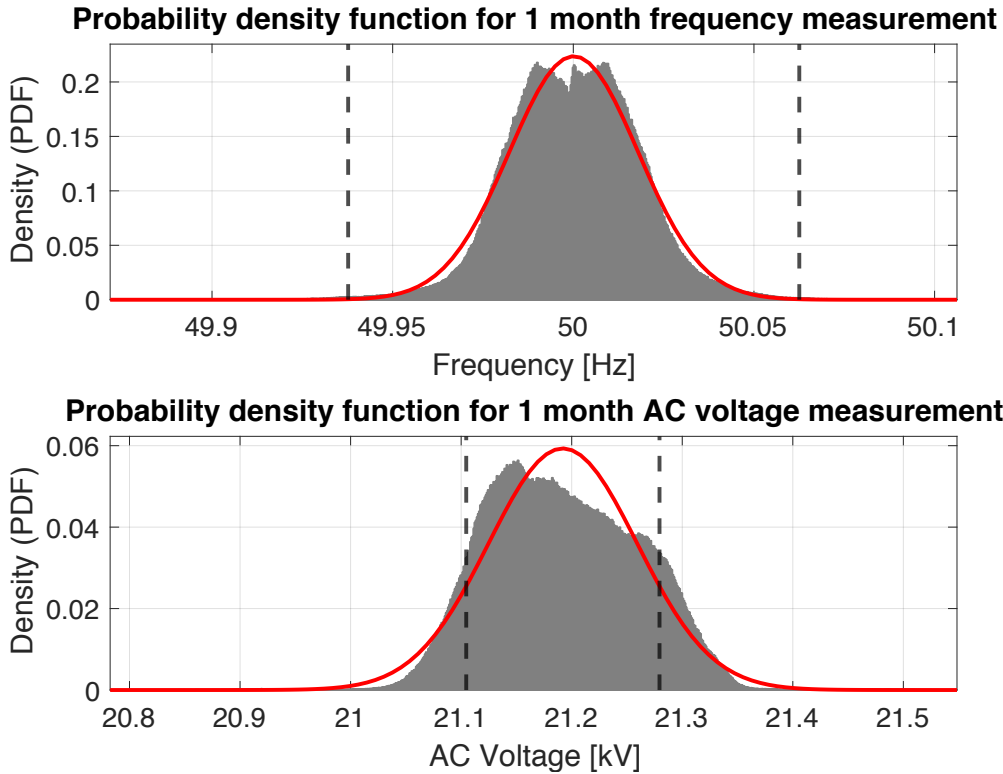


**Figure 2.6:** 1 month historical data of frequency and phase-to-phase voltage at the BESS PCC at 21 kV, acquired via PMUs installed at the EPFL MV network. The dashed lines represent the limits of  $\mu_f \pm 3.3\sigma_f$  and  $\mu_V \pm 1\sigma_V$  for frequency and voltage measurements, respectively.

## 2.3. Experimental investigation

A number of scenarios have been investigated considering different combinations of initial droops  $\alpha_0$  and  $\beta_0$ . Table 2.5 reports the overview of the analysed cases. It should be noted that, in addition to different initial droops  $\alpha_0$  and  $\beta_0$ , what also changes are network conditions (i.e., grid frequency and voltage) that we do not control. Each test has been carried out for a 5-minute time window, and the real-time BESS battery and AC grid statuses have been monitored and processed in order to compute the optimal P and Q set-points as described in Section II. The same priority has been given to the provision of P and Q by setting  $\lambda_P=\lambda_Q=1$  in the implementation of Eq. (2.14). A time granularity of 1 second has been used for data acquisition and optimal set-point computation, meaning that at each second a new operating point within the corresponding feasible PQ region is sent to the BESS converter controller. The choice of 1-second response is considered as a realistic assumption in BESS applications as indicated, for instance, by the newly-released grid code by the Danish TSO Energinet.dk [19]. However, the Authors are aware that in low-inertia power systems rapid (i.e., sub-second) frequency variations are more likely to be experienced [20], meaning that even faster response from control providers may be needed.

**Table 2.5:** Calculated  $\alpha_0$  and  $\beta_0$  for different shrink factors  $C_{shrink}$

<i>Scenario</i>	$\alpha_0$	$\beta_0$
#1	9003 [kW/Hz]	8.39 [kvar/V]
#2	9905 [kW/Hz]	8.39 [kvar/V]
#3	19810 [kW/Hz]	8.39 [kvar/V]
#4	29715 [kW/Hz]	12.57 [kvar/V]

Fig. 2.7 shows results for *Scenario#1*, for which  $\alpha_0$  and  $\beta_0$  are calculated as in the previous Subsection. The top subplots of (a) and (b) report the measured AC grid frequency and the mean value of the three phase-to-phase voltages at the MV connection point, with the respective reference values used for the calculation of  $\Delta f_t$  and  $\Delta v_t^{AC}$  as in Eq. (2.1). The computed P-Q set-point calculated implementing the standard droop control equation in Eq. (2.1) are reported in red in the bottom subplots. Additionally, the actual set-points computed as result of the optimization problem are shown with the blue lines. Note that, as already stated in Section II, for the selection of the appropriate converter PQ capability curve at each time-step, the AC voltage measured at the 21 kV busbar is scaled down to the LV side voltage level of the BESS step-up transformer using the associated transformation ratio. Firstly, it can be seen that for frequency measurements larger than 50 Hz, the BESS behaves as a load: the sign of the exchanged active power is negative, meaning that the BESS is charging. Symmetrically, when the frequency is below the 50 Hz, the BESS discharges by injecting active power with positive sign into the grid. Similar considerations are valid for the local voltage control. In general, for  $\Delta v^{AC} > 0$ , i.e., in case of over-voltages, negative reactive power is provided by the BESS, meaning that the BESS behaves as an inductor. On the contrary, for  $\Delta v^{AC} < 0$ , i.e., in case of under-voltages, capacitive reactive power is provided, as in the case of the whole time-window for the test of *Scenario#1*. Secondly, it can be noticed that the desired frequency containment reserve is fully achieved since the expected active power is provided at any moment of the considered time window. By contrast, the relatively large value of the initial droop  $\beta_0$  and the measured deviations of the AC voltage from the reference value, caused a mismatch between the expected and the provided voltage control service for more than half of the time of the test. In fact, in these cases the desired Q set-point would have been out of the feasible region of the employed hardware, hence the proposed optimal control approach moved it to the edge of the corresponding PQ capability curve.

The test for *Scenario#2* presented in Fig. 2.8 shows a case when the local voltage control via reactive power is achieved continuously, although the implemented initial droop  $\beta_0$  is the same as in

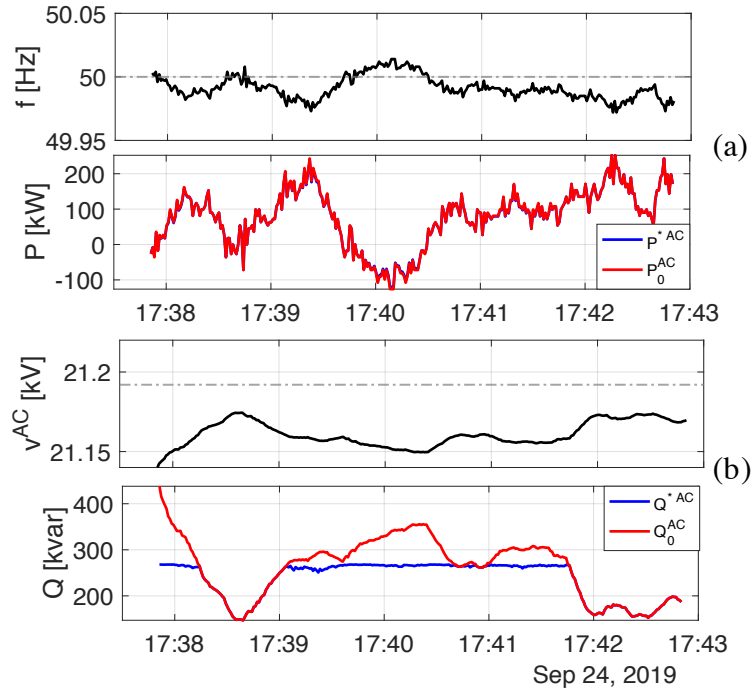


**Figure 2.7:** *Scenario#1* Results. (a): FCR; (b): local voltage control.

*Scenario#1*. Also the frequency containment reserve action is performed continuously, responding as desired to the measured frequency signal for the whole duration of the test. In this case a larger initial droop  $\alpha_0$  was implemented, namely a value calculated considering  $\pm 3\sigma_f$  as the maximum frequency deviation, i.e., with a confidence interval of 99.7%.

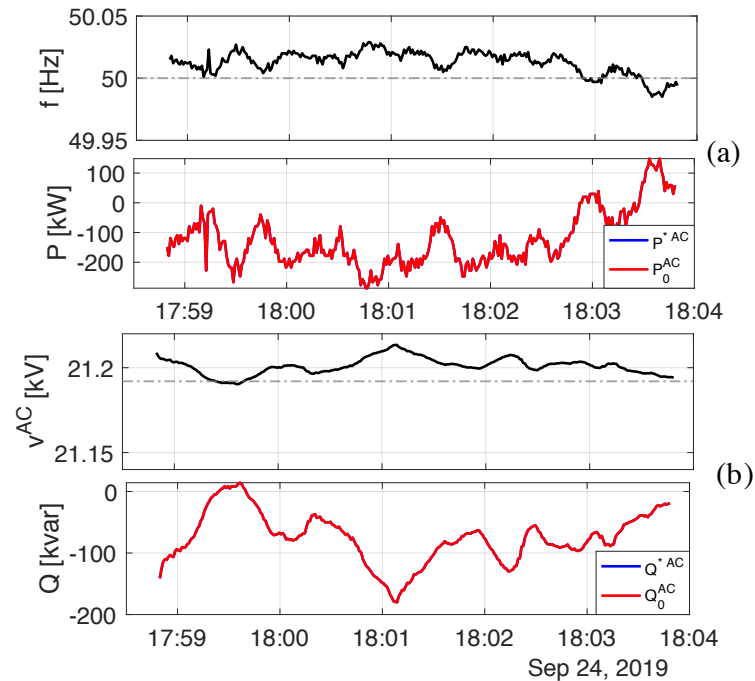


**Figure 2.8:** *Scenario#2* Results. (a): FCR; (b): local voltage control.

In *Scenario#3* an even larger value of  $\alpha_0$  was used, corresponding to  $\pm 1.5\sigma_f$  as the maximum

frequency deviation, i.e., with a confidence interval of 86.6%. In this test case, the solution of the optimization problem enabled the BESS to operate also when the calculated P set-points falls outside the feasible region of the considered PQ capability curve. In fact, the values at the edge of the feasible region were set, meaning that the frequency service was not performing as desired, although the maximum power was still provided to partially support the grid. From Fig. 2.9, it can be seen that this happens in the first 38 seconds of the test and for a shorter period of time also around the mid point. Fig. 2.9-(c) maps the operating points before and after the implementation of the proposed optimal set-point calculation. It can be noticed that, thanks to the proposed method, the points falling outside the feasible region have been retrieved to the edge of the light blue converter feasible region, thus assuring the continuity of the delivery of the two grid services. Furthermore, it is of paramount importance to note that without the proposed optimal controller the too high value of the computed P set-point would have made the BESS converter either trip or go to 0 kW for safety reasons. Under these circumstances, the expected service would have been fully undelivered, enhancing the probability of reaching the 0.1% threshold imposed by the Swiss TSO for undelivered regulating power when providing frequency containment reserve. It is in fact relevant to quantify the amount of regulating energy actually delivered during the regulation session and to compare it with the energy that would have been delivered without optimization and in the ideal case of unconstrained BESS power converter. So, the quantification - as for FCR provision - of the concrete effects of the proposed controller with control time granularity  $\Delta t$  during a control session of duration  $T\Delta t$  is done as described in Eq. (2.17)-Eq. (2.19). They define the expected energy  $E_{exp}$ , the actual delivered energy with the optimal control  $E^*$ , and the energy that would have been delivered without the proposed optimal approach  $E_0$ , respectively. Such quantification is included in Table 2.6.

$$E_{exp} = \sum_{i=1}^T \Delta t |\alpha_0 \Delta f_i| \quad (2.17)$$

$$E^* = \sum_{i=1}^T \Delta t |P_i^{*AC}| \quad (2.18)$$

$$E_0 = \sum_{i=1}^T \Delta t |P_{0,i}^{AC}| \quad (2.19)$$

Finally, *Scenario#4* is analysed to assess the situation in case of a very large initial droops  $\alpha_0$  and  $\beta_0$ , corresponding to maximum deviations of  $\pm 1.5\sigma_f$  and  $\pm 0.75\sigma_V$ . Although the very low measured voltage deviations made the computed Q set-point be inside the feasible PQ region all the time, the same is not valid for P. In fact, Fig. 2.10 shows that for almost the whole duration of the test, the P set on the converter is at the edge of the selected feasibility curve, meaning that the frequency containment grid service is not fully delivered. The mapping of the PQ set-points before and after the solution of the proposed optimization problem is shown in Fig. 2.10-(c). As for *Scenario#3*, the continuity of the delivery of the two grid services is possible thanks to the projection of the initially-calculated set-points to the edge of the light blue converter feasible region. The quantification of the effectiveness of the optimal controller in terms of expected and delivered regulating energy is reported in Table 2.6.

To conclude, the work presented a BESS control framework for optimal provision of concurrent power system services. In particular, frequency containment reserve provision and local voltage control are achieved via the modulation of active and reactive power set-points, respectively, exploiting the flexibility given by the 4 quadrant power converter. The proposed algorithm considers the working conditions of the AC utility grid as well as the battery DC voltage as a function of the current trajectory

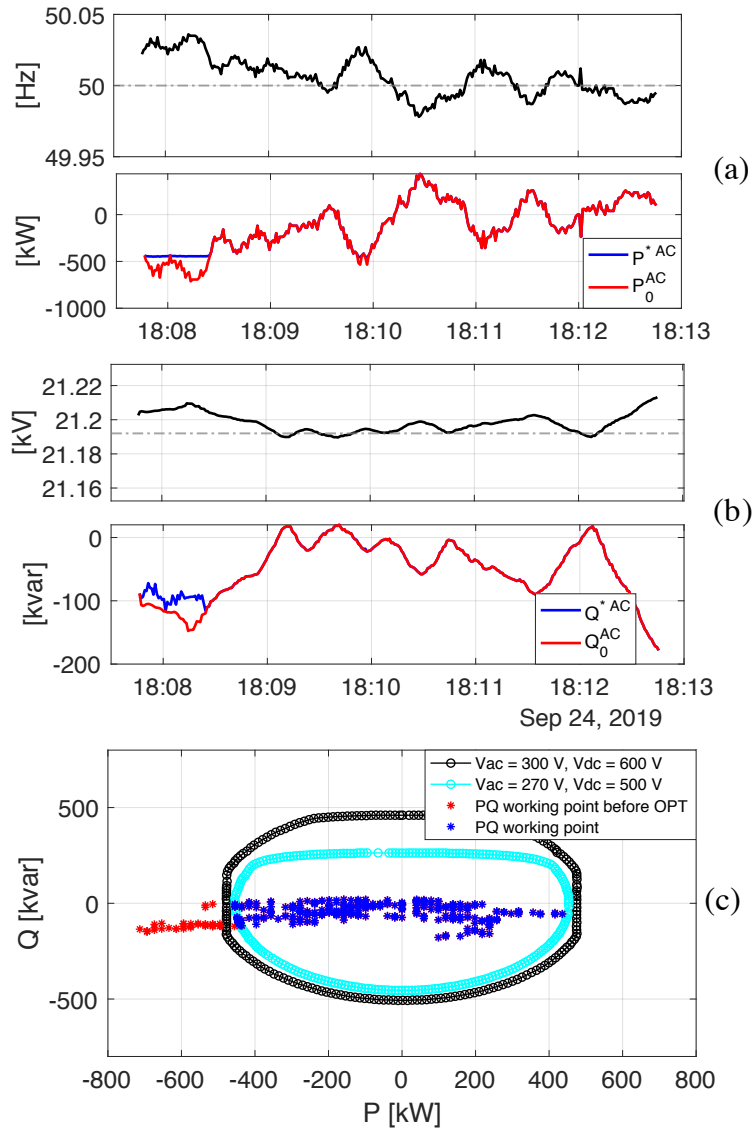


**Figure 2.9:** Scenario#3 Results. (a): FCR; (b): local voltage control; (c): PQ set-points before and after the proposed optimization algorithm.

**Table 2.6:** Expected and delivered energy for FCR with and without the proposed optimization algorithm

Scenario	$E_{exp}$	$E^*$	$E_0$
#1	8.3 [kWh]	8.3 [kWh]	8.3 [kWh]
#2	10.5 [kWh]	10.5 [kWh]	10.5 [kWh]
#3	20.0 [kWh]	18.4 [kWh] (91.90%)	13.7 [kWh] (68.47%)
#4	45.7 [kWh]	35.0 [kWh] (76.49%)	9.1 [kWh] (19.91%)

using the battery TTC model, in order to select the suitable converter capability curve, which is not unique for all the possible operating conditions, hence optimizing the provision of grid services. A computationally-efficient algorithm was proposed to solve the formulated optimal power set-points

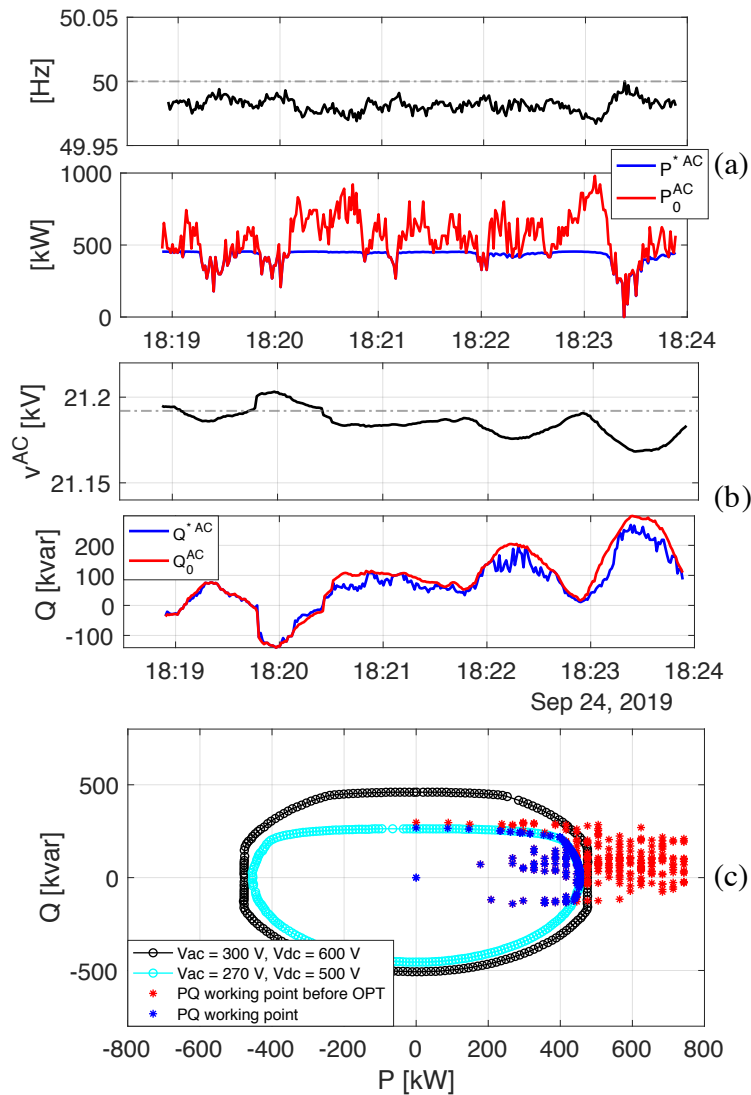


**Figure 2.10:** *Scenario#4* Results. (a): FCR; (b): local voltage control; (c): PQ set-points before and after the proposed optimization algorithm.

calculation problem.

A set of experimental tests on a commercial utility-scale 720 kVA/560 kWh BESS showed the capability of the controller to enable PFC and local voltage control not only by charging or discharging the battery, but also by means of reactive power exchange, namely behaving as inductor or capacitor in case of over- or under-voltages, respectively. When in case of large initial droop constants or large frequency/voltage deviations the PQ feasible region is passed, the proposed controller enabled the operation at the edge of the selected PQ capability curve, dramatically reducing the amount of accumulated non-delivered regulating power during the control session. Hence, this Chapter highlighted the importance of accurately modelling the employed hardware in order to enable an optimal grid service provision even under non-nominal BESS conditions (e.g., reduced available number of strings) as well as under commercial hardware embedded technical limitations (e.g., variable capability curves of the power converter).

Future works include the extension of the complexity of the model by considering the power conversion efficiency as a function of the exchanged AC active power, and a series of experimental tests to map more systematically all the possible capability curves for a wider range of combinations of

---

battery DC voltage and grid voltage conditions. Further, investigations on BESS control logics as voltage source in combination with the provision of ancillary services are of interest.

### 3. Optimal grid-forming control of a battery energy storage system providing multiple services

This Chapter proposes and experimentally validates a joint control and scheduling framework for a grid-forming converter-interfaced BESS providing multiple services to the electrical grid. The framework is designed to dispatch the operation of a distribution feeder hosting heterogeneous prosumers according to a dispatch plan and simultaneously provide frequency containment reserve, inertial response, voltage control and system strength as ancillary services [13]. The framework consists of three phases. In the day-ahead scheduling phase, a robust optimization problem is solved to compute the optimal dispatch plan and frequency droop coefficient, accounting for the uncertainty of the aggregated prosumption. In the intra-day phase, a model predictive control algorithm is used to compute the power set-point for the BESS to achieve the tracking of the dispatch plan. Finally, in a real-time stage, the power set-point originated by the dispatch tracking is converted into a feasible frequency set-point for the grid forming converter by means of a convex optimisation problem accounting for the capability curve of the power converter. The proposed framework is experimentally validated by using a grid-scale 720 kVA/560 kWh BESS connected to a 20 kV distribution feeder of the EPFL hosting stochastic prosumption and PV generation.

NOTE: *The content of this Section has been published within the framework of the Osmose project: Francesco Gerini, Yihui Zuo, Rahul Gupta, Elena Vagnoni, Rachid Cherkaoui, Mario Paolone, "Optimal Grid-Forming Control of Battery Energy Storage Systems Providing Multiple Services: Modeling and Experiment Validation", to be presented at 2022 Power System Computation Conference, Porto, Portugal.*

*Emil Namor, Fabrizio Sossan, Rachid Cherkaoui and Mario Paolone, "Control of Battery Storage Systems for the Simultaneous Provision of Multiple Services," in IEEE Transactions on Smart Grid, vol. 10, no. 3, pp. 2799-2808, May 2019.*

#### 3.1. Problem statement

The dispatchability of distribution feeders and the simultaneous provision of FCR and voltage regulation is tackled by controlling a grid-forming converter-interfaced BESSs. Specifically, it is ensured the control of the operation of a group of prosumers (characterized by both conventional demand and PV generation that are assumed to be uncontrollable) according to a scheduled power trajectory at 5 minutes resolution, called dispatch plan, determined the day before operation. The day-ahead scheduler relies on a forecast of the local prosumption. The multiple-service-oriented framework are summarized by Figure 3.1. It consists of three stages, each characterised by different time horizons:

1. The dispatch plan is computed on the day-ahead (i.e., in agreement with most common practice), where the feeder operator determines a dispatch plan based on the forecast of the prosumption while accounting also for the regulation capacity of BESSs [21]. By referring to state-of-the-art practice applied to FCR of *Transmission System Operators* (TSO) of France, Germany, Belgium, the Netherlands, Austria and Switzerland [22], [23], the FCR is supposed to be allocated on a daily basis and the GFM droop is computed accordingly. For these reasons, in the day-ahead stage, an optimization problem is solved to allocate the battery power and energy budgets to the different services by determining a dispatch plan at a 5-minute resolution based on the forecast of the prosumption and computing the droop for the FCR provision. The dispatch plan is the sum of two terms: the forecasted power profile of the feeder prosumption and an offset power profile computed to keep the BESS SOC within proper limits.
2. In the intermediate level stage, with a 5-minute horizon, the active power injections of the BESS

are adjusted by means of a MPC targeting both the correction of the mismatch between prosumption and dispatch plan (as proposed by [5]) and the FCR provision. The MPC is actuated every 10 seconds to both ensure a correct tracking over the 5 minutes window and avoid overlapping the dispatch tracking with the FCR action.

3. In the final stage, computed each second, the MPC active power and reactive power commands are converted into a feasible frequency and voltage set-points for the GFM converter. As a matter of fact, the feasible PQ region of the BESS power converter is a function of the battery DC-link and AC-grid status [24]. For this reason, the feasibility of the grid-forming frequency and voltage reference set-points is ensured by solving every second an efficient optimization problem that takes into account the dynamic capability curve of the DC-AC converter and adjusts the set point accordingly. The initial power set-points are obtained based on the traditional droop control approach, superimposed with the set-point originated by the MPC problem. Due to the final power set-points calculation is formulated as a non-convex optimization problem, a convex reformulation of the original control problem is proposed to give the global optimal solution to the initial non-convex problem. Eventually, the feasible frequency and voltage set-points are implemented in the GFM controller which intrinsically superposes the frequency control action on the active power dispatch.

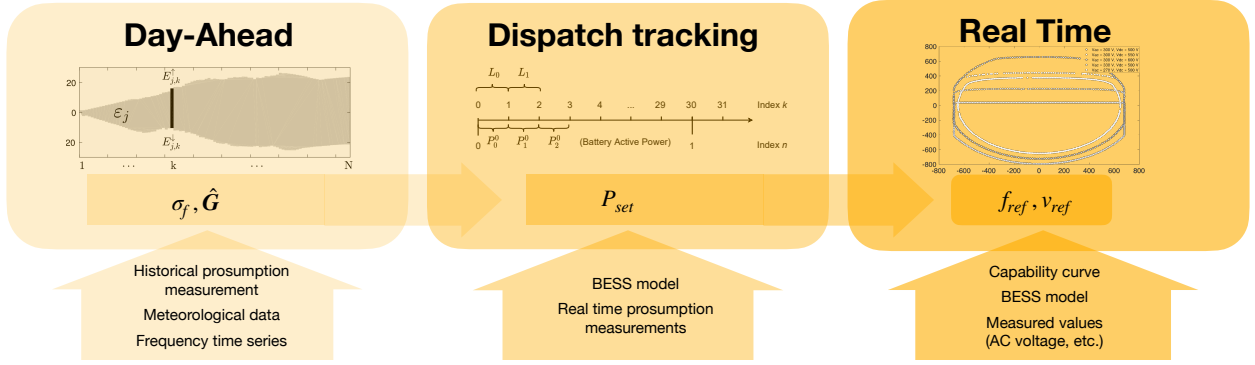


**Figure 3.1:** Control Scheme for grid forming control

It is worth clarifying that the first two stages (i.e., day-ahead and dispatch tracking) are not exclusively for the GFM mode. They are also applicable for GFL controllers to achieve the multiple-service objective, i.e., dispatching and FCR provision.

## 3.2. Multiple-services control framework for a BESS operating in grid-forming mode

### 3.2.1. Day-Ahead Stage

The objective of the day ahead is to compute a dispatch plan  $\hat{G}$  for a distribution feeder and to simultaneously contract with the TSO a certain frequency droop, for the BESS FCR provision. A representation of the feeder and the corresponding power flows is shown in Fig. 3.2.

The BESS bidirectional real power flow is denoted by  $P$ , while  $G$  is the composite power flow as seen at the *Point of Common Coupling* (PCC). The aggregated building demand is denoted by  $L$  and, by neglecting grid losses, it is estimated as:

$$L = G - P \quad (3.1)$$

Further to the achievement of feeder dispatchability, the proposed framework allows the GFM-

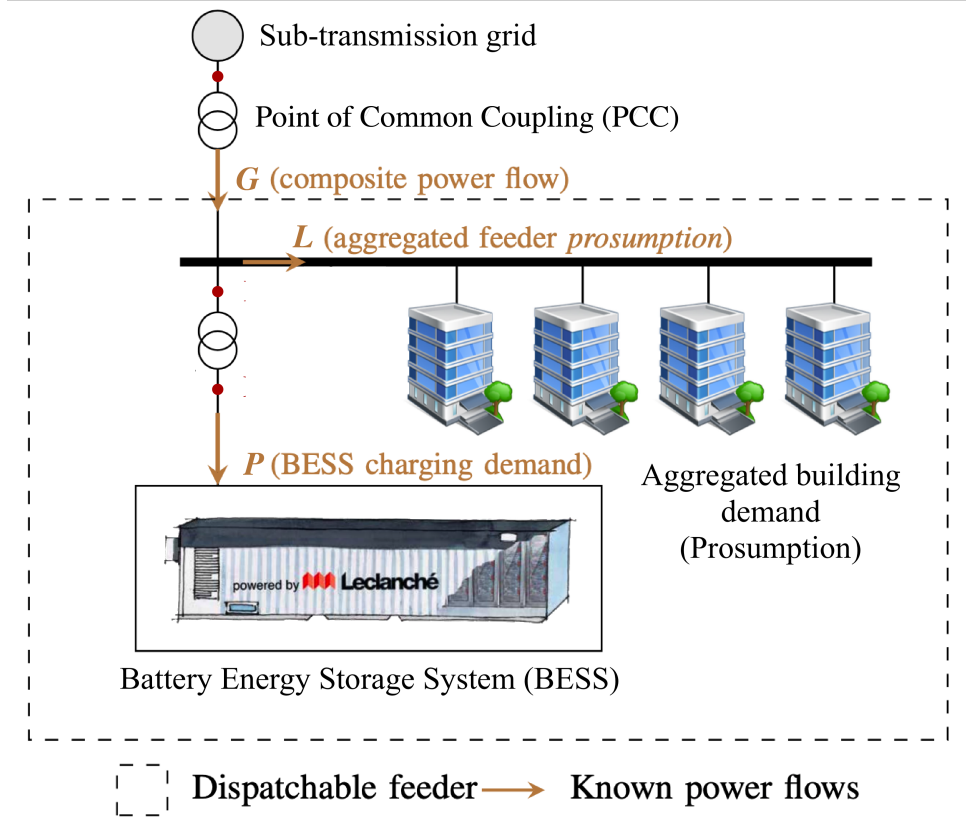


**Figure 3.2:** Topology of the feeder for the problem statement

controlled BESS to react against the grid-frequency variation in real time, i.e., providing inertial response on top of the FCR. The latter action is automatically performed by the converter operated in GFM mode, where the power flowing from to the BESS can be computed as:

$$P = \sigma_f \cdot (f - f_{ref}) \quad (3.2)$$

$$Q = \sigma_v \cdot (v - v_{ref}) \quad (3.3)$$

In Eq. (3.2) and Eq. (3.3)  $\sigma_f$  and  $\sigma_v$ <sup>1</sup> are respectively the frequency and voltage droop fixed at the day-ahead stage, while  $f_{ref}$  and  $v_{ref}$  are the frequency and voltage reference set-point (i.e., real-time command) of the GFM converter. The target of the control problem is to regulate the composite power flow  $G$  to respect the dispatch plan fixed on the day-ahead planning and the frequency containment action accorded with the TSO.

The formulation of the day-ahead problem considering the provision of both FCR and dispatchability

<sup>1</sup>While the  $\sigma_f$  is computed in the day-ahead problem for the FCR service, the  $\sigma_v$  is considered to allow for adjusting reactive power in the real-time stage (see in Section 3.2.3) and is determined according to the voltage control practice recommend in [23].

by [4] can be adapted to the grid-forming case. The mathematical formulation is hereby proposed:

$$[\sigma_f^0, \mathbf{F}^0] = \arg \max_{\sigma_f \in \mathbb{R}^+, \mathbf{F} \in \mathbb{R}^N} (\sigma_f) \quad (3.4a)$$

subject to:

$$SOC_0 + \frac{1}{E_{\text{nom}}} \left[ \frac{T}{N} \sum_{i=0}^n (F_i + L_i^\uparrow) + \sigma_f W_{f,n}^\uparrow \right] \leq SOC_{\text{max}}, \quad (3.4b)$$

$$SOC_0 + \frac{1}{E_{\text{nom}}} \left[ \frac{T}{N} \sum_{i=0}^n (F_i + L_i^\downarrow) + \sigma_f W_{f,n}^\downarrow \right] \geq SOC_{\text{min}}, \quad (3.4c)$$

$$F_n + L_n^\uparrow + 0.2\sigma_f \geq P_{\text{max}}, \quad (3.4d)$$

$$F_n + L_n^\downarrow + 0.2\sigma_f \leq P_{\text{max}}, \quad (3.4e)$$

where:

- $T$  is the total scheduling time window (i.e.,  $T = 86400$  seconds) discretized in  $N$  time steps ( $N = 288$ , i.e., the dispatch plan is divided into 5 minutes windows) and each step is denoted by the subscript  $n$  with  $n = 0, \dots, N - 1$ .
- $\hat{\mathbf{L}} = \hat{L}_1, \dots, \hat{L}_N$  is the forecast profile of feeder prosumption.  $\mathbf{L}^\uparrow = L_1^\uparrow, \dots, L_N^\uparrow$  and  $\mathbf{L}^\downarrow = L_1^\downarrow, \dots, L_N^\downarrow$  are the highest and lowest scenarios of the forecasted prosumption, respectively.  $\mathbf{F}^0 = F_1, \dots, F_N$  is the BESS power offset profile which is computed to keep the BESS stored energy at a value capable to compensate for the difference between prosumers' forecasted and realized power. The day-ahead dispatch plan  $\hat{\mathbf{G}} = \hat{G}_1, \dots, \hat{G}_N$  is the sum of the forecasted power profile of the feeder prosumption  $\mathbf{L}$  and the offset power profile  $\mathbf{F}^0$ , as in Eq. (3.1).
- $\sigma_f$  is the FCR droop expressed in kW/Hz.
- $W_{f,n}$  denotes the integral of frequency deviations over a period of time (i.e., 5 minutes), and it represents the energy content of the signal given by the frequency deviation from its nominal value. Therefore,  $\sigma_f W_{f,n}$  represents the energy required from the BESS for the primary frequency regulation.  $W_{f,n}^\uparrow$  and  $W_{f,n}^\downarrow$  are respectively the upper and lower bounds of the integrated frequency deviation at time interval  $n$ .
- The BESS limits in terms of *State Of Charge* (SOC) and power are expressed respectively with  $SOC_{\text{min}}$ ,  $SOC_{\text{max}}$ ,  $P_{\text{min}}$  and  $P_{\text{max}}$ , while  $E_{\text{nom}}$  is the nominal BESS energy.

It is worth mentioning that the optimization problem described by Eqs. (3.4a) to (3.4e) prioritizes the dispatchability of the feeder over the FCR provision on the day-ahead planning. This choice is nevertheless user-dependent, based on the economical convenience of the provided services. For example, if the user stipulates a contract with the TSO for FCR provision, this service can be prioritized, and the remaining energy can be allocated for the dispatch service, that will inevitably not be always achieved if the prosumption stochasticity is too high<sup>2</sup>.

### 3.2.2. Intra-day Stage

In the intra-day stage a MPC algorithm is used to target the fulfillment of the mismatch between average prosumption for each 5-minute period and dispatch plan plus FCR action accorded with the TSO for the same time-window. Since the MPC action has a time-sampling of 10 seconds, the index  $k = 0, 1, 2, \dots, K - 1$  is introduced to denote the rolling 10 seconds time interval, where  $K = 8640$  is the number of 10 second periods in 24 hours. The value of the prosumption set-point retrieved from

<sup>2</sup>Further discussion can be found in Section 3.3.

the dispatch plan for the current 5-minute slot is indicated by the  $k$ -index as:

$$G_k^* = \hat{G}_{\lfloor \frac{k}{30} \rfloor} \quad (3.5)$$

where  $\lfloor \cdot \rfloor$  denotes the nearest lower integer of the argument, and 30 is the number of 10-second interval in a 5-minute slot. The first and the last 10-second interval for the current 5-minutes are denoted as  $\underline{k}$  and  $\bar{k}$ , respectively:

$$\underline{k} = \lfloor \frac{k}{30} \rfloor \cdot 30 \quad (3.6)$$

$$\bar{k} = \underline{k} + 30 - 1 \quad (3.7)$$

A graphical representation of the execution timeline for the MPC problem is given by Fig. 3.3 displaying the first thirty-one 10-seconds intervals of the day of operation. The figure shows the BESS power set-point  $P_2^o$ , which has been computed by knowing the prosumption realizations  $L_0$  and  $L_1$ , and the average prosumption set-point to be achieved in the 5-minute interval (i.e., first value of the dispatch plan  $\hat{G}_0$ ).

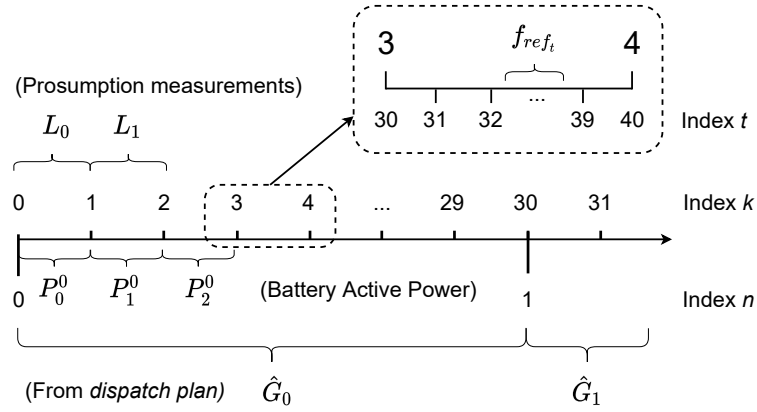


**Figure 3.3:** Timeline for the MPC problem

A similar control problem, not including the simultaneous provision of FCR by the BESS, is described in [5]. For this reason, the MPC problem proposed in [5] is modified as follows, to account for the provision of multiple services by means of GFM converter. Considering Eq. (3.1), the average composite power flow at the PCC (prosumption + BESS injection) is given by averaging the available information until  $k$  as:

$$G_k = \frac{1}{k - \underline{k}} \cdot \sum_{j=\underline{k}}^{k-1} (L_j + P_j) \quad (3.8)$$

Then, it is possible to compute the expected average composite flow at the PCC at the end of the 5 minutes window as:

$$G_k^+ = \frac{1}{30} \left( (k - \underline{k}) \cdot G_k + \sum_{j=\underline{k}}^{\bar{k}} \hat{L}_{j|k} \right) \quad (3.9)$$

where a persistent<sup>3</sup> forecast is used to model future realizations, namely  $\hat{L}_{j|k} = L_{k-1}, j = k, \dots, \bar{k}$ . The energy error between the realization and the target (i.e. dispatch plan plus FCR energy) in the

<sup>3</sup>As shown in [25], the persistent predictor performs well given the short MPC horizon time and fast control actuation in this application.

5-minute slot is expressed (in kWh) as:

$$e_k = \frac{300}{3600} \cdot (G_k^* - G_k^+ + \Delta G_k^F) \quad (3.10)$$

where 300 s and 3600 s are the number of seconds in a 5 minutes interval and 1 hour interval, respectively. The additional term  $\Delta G_k^F$  considers the deviation caused by the frequency containment response of the GFM converter:

$$\Delta G_k^F = \frac{1}{30} \sum_{j=k}^{k-1} (50 - f_j) \cdot \sigma_f \quad (3.11)$$

where  $f_j$  is the frequency measurement at time  $j$ . Finally, the MPC can be formulated to minimize the error  $e_k$  over the 5-minutes window, subject to a set of physical constraints such as BESS SOC, DC voltage and current operational limit. It should be noted that including the term  $\Delta G_k^F$  in the energy error function fed to the MPC allows for decoupling the dispatch plan tracking with the frequency containment response provided by the BESS in each 5-minute slot. In particular, the omission of this term while operating the BESS in GFM mode, can create conflicts between dispatch plan tracking and frequency containment provision. As in [5], in order to achieve a convex formulation of the optimization problem, the proposed MPC problem targets the maximisation of the sum of the equally weighted BESS DC-side current values over the shrinking horizon from  $k$  to  $\bar{k}$  in its objective (3.12a) while constraining the total energy throughput to be smaller or equal to the target energy  $e_k$ . The optimization problem is formulated as:

$$\mathbf{i}_{\bar{k}|k}^o = \arg \max_{\mathbf{i} \in \mathbb{R}^{(k-\bar{k}+1)}} (\mathbf{1}^T \mathbf{i}_{\bar{k}|k}) \quad (3.12a)$$

subject to:

$$\alpha \mathbf{v}_{\bar{k}|k}^T \mathbf{i}_{\bar{k}|k} \leq e_k \quad (3.12b)$$

$$\mathbf{1} \cdot i_{min} \preceq \mathbf{i}_{\bar{k}|k} \preceq \mathbf{1} \cdot i_{max} \quad (3.12c)$$

$$\mathbf{1} \cdot \Delta i_{min} \preceq H \mathbf{i}_{\bar{k}|k} \preceq \mathbf{1} \cdot \Delta i_{max} \quad (3.12d)$$

$$\mathbf{v}_{\bar{k}|k} = \phi_v x_k + \psi_i^v \mathbf{i}_{\bar{k}|k} + \psi_1^v \mathbf{1} \quad (3.12e)$$

$$\mathbf{1} \cdot v_{min} \preceq \mathbf{v}_{\bar{k}|k} \preceq \mathbf{1} \cdot v_{max} \quad (3.12f)$$

$$SOC_{\bar{k}|k} = \phi^{SOC} SOC_k + \psi_i^{SOC} \mathbf{i}_{\bar{k}|k} \quad (3.12g)$$

$$\mathbf{1} \cdot SOC_{min} \preceq SOC_{\bar{k}|k} \preceq \mathbf{1} \cdot SOC_{max} \quad (3.12h)$$

where

- $\mathbf{i}_{\bar{k}|k}^o$  is the computed control action trajectory,  $\mathbf{1}$  denotes the all-ones column vector, the symbol  $\preceq$  is the component-wise inequality, and the bold notation denotes the sequences obtained by stacking in column vectors the realizations in time of the referenced variables, e.g.  $\mathbf{v}_{\bar{k}|k} = [v_k, \dots, v_{\bar{k}}]^T$ .
- In (3.12b), the BESS energy throughput (in kWh) on the AC bus is modeled as  $E_{\bar{k}|k}(\cdot) = \alpha \mathbf{v}_{\bar{k}|k}^T \mathbf{i}_{\bar{k}|k}$ , where  $\mathbf{v}_{\bar{k}|k}$  and  $\mathbf{i}_{\bar{k}|k}$  are the battery DC voltage and current, respectively, and  $\alpha = 10/3600$  is a converting factor from average power over 10 seconds to energy expressed in kWh.
- The inequality (3.12c) and (3.12d) are the constraints on the magnitude and rate of change for

the BESS current, respectively. The matrix  $H \in \mathbb{R}^{(k-\bar{k}+1) \times (k-\bar{k}+1)}$  is

$$H = \begin{bmatrix} 1 & -1 & 0 & 0 & \dots & 0 \\ 0 & 1 & -1 & 0 & \dots & 0 \\ \vdots & \vdots & \vdots & \vdots & \vdots & \vdots \\ 0 & 0 & 0 & \dots & 1 & -1 \end{bmatrix} \quad (3.13)$$

- The equality (3.12e) is the *Three-Time-Constant (TTC)* electrical equivalent circuit model of the voltage on DC bus, whose dynamic evolution can be expressed as a linear function of battery current by applying the transition matrices  $\phi^v, \psi^v, \psi_1^v$ .  $x_k$  is the state vector of the voltage model. The inequality (3.12f) defines the BESS voltage limits. The TTC model for computing the DC voltage and the estimation of  $x_k$  are described in [5].
- The equality (3.12g) is the evolution of the BESS SOC as linear function of the variable  $i_{\bar{k}|k}^o$ , where  $\phi^{SOC}$  and  $\psi_i^{SOC}$  are transient matrices obtained from the BESS SOC model:

$$SOC_{k+1} = SOC_k + \frac{10}{3600} \frac{i_k}{C_{nom}} \quad (3.14)$$

where  $C_{nom}$  is BESS capacity in [Ah]. The discretized state-space matrix for the SOC model can be easily obtained from (3.14) with  $A_s = 1$ ,  $B_s = 10/3600/C_{nom}$ ,  $C_s = 1$ ,  $D_s = 0$ . Finally, (3.12h) enforces the limits on BESS SOC.

The optimization problem is solved at each time step  $k$  obtaining the control trajectory for the whole residual horizon from the index  $k$  to  $\bar{k}$ , i.e.,  $i_{\bar{k}|k}$ . However, only the first component of the current control trajectory is considered for actuation, i.e.,  $i_{\bar{k}|k}^o$ . Then,  $i_{\bar{k}|k}$  is transformed into a power set-point  $P_k^0$ , computed as:

$$P_k^0 = v_k \cdot i_k^o \quad (3.15)$$

### 3.2.3. Real-Time Control Stage

The real-time control stage is the final stage of the framework, whose output  $f_{ref}, v_{ref}$  is the input for the GFM BESS converter. Thanks to the day-ahead problem, sufficient BESS energy capacity is guaranteed in the MPC tracking problem. To ensure the BESS operation to be within the power limits, a static physical constraint of control actions is considered in the day-ahead stage in (3.4d) and (3.4e) and during the dispatch tracking in (3.12c) and (3.12d). Nevertheless, these constraints do not account for the dependency of the converter feasible PQ region on DC voltage and AC grid voltage conditions since they are only known in reality. In this respect, the real-time controller is implemented to both keep the converter operating in the PQ feasible region identified by the capability curve and to convert the power set-point from the MPC problem into a frequency reference set-point to feed the GFM converter.

#### 3.2.3.1. Capability Curve

As discussed in [24] and in the previous chapter, the converter PQ capability curve  $h$  can be modelled as a function of the BESS DC voltage  $v_t^{DC}$  and the module of the direct sequence component of the phase-to-phase BESS AC side voltages  $v_t^{AC}$  at time  $t \in [1, 2, \dots, T]$  as:

$$h(P_t, Q_t, v_t^{DC}, v_t^{AC}, SOC_t) \leq 0 \quad (3.16)$$

where the BESS SOC is considered for the selection of the capability curve because the estimation of  $v_t^{DC}$  relies on the battery TTC model whose parameters are SOC-dependent [24]. In particular, the  $v_t^{DC}$  is estimated using the TTC model of DC voltage, thus, the same formula as (3.12e):

$$v_t^{DC} = \phi_v x_t + \psi_i^v i_t^{DC} + \psi_1^v \mathbf{1} \quad (3.17)$$

Equation (3.17) is solved together with the charging or discharging DC current equation as follows:

$$i_t^{DC} \approx \frac{P_t^{DC}}{v_t^{DC}} \quad (3.18)$$

where the active power at the DC bus is related to the active power set-point AC side of the converter as:

$$P_t^{DC} = \begin{cases} \eta P_{set,t}, & \forall P_{set,t} < 0 \\ P_{set,t}/\eta, & \forall P_{set,t} \leq 0 \end{cases} \quad (3.19)$$

where  $\eta$  is the efficiency of converter,  $P_{set,t}$  is the set-point from the MPC, computed in (3.15) and expressed as:

$$P_{set,t} = P_{\lfloor \frac{t}{10} \rfloor}^0 \quad (3.20)$$

Once the DC voltage  $v_t^{DC}$  is known, the magnitude of the direct sequence component  $v_t^{AC}$  of the phase-to-phase voltage at AC side of the converter is estimated via the Thévenin equivalent circuit of the AC grid, expressed as

$$v_t^{AC} \approx \sqrt{(v_t^{AC,m})^2 + X_T^2 \frac{(P_{set,t})^2 + (Q_{set,t})^2}{3(v_t^{AC,m})^2}} \quad (3.21)$$

where the primary side voltage  $v_t^{AC,MV}$  is referred to the secondary side as  $v_t^{AC,m} = v_t^{AC,MV} \frac{1}{n}$ , being  $n$  the transformer ratio,  $v_t^{AC,MV}$  is the voltage measured at the primary side of the transformer, and  $X_T$  is the reactance of the step-up transformer, as shown in Fig. 3.2. Equations (3.16) to (3.21) represent the relation between active and reactive power set-points with the converter capability curve.

### 3.2.3.2. Set-point conversion for GFM converters

Together with a feasibility check for the power set-point  $P_{set,t}$ , the real time controller is responsible for converting the power set-point into a frequency reference set-point to feed the GFM converter. In particular, the power output of a GFM converter can be expressed, starting from Eq. (3.22), as:

$$P = \sigma_f \cdot (f - f_{nom}) + \sigma_f \cdot (f_{nom} - f_{ref,t}) = P_{fcr} + P_{set,t} \quad (3.22)$$

where  $f_{nom}$  is the nominal frequency, the term  $P_{fcr}$  corresponds to the power delivered with respect to the frequency containment action,  $f$  is the grid frequency<sup>4</sup>. As visible from Equation (3.22), the relation between the power set-point  $P_{set}$  of the GFM converter and the input  $f_{ref}$  is linear:

$$P_{set,t} = \sigma_f \cdot (f_{nom} - f_{ref,t}) \quad (3.23)$$

<sup>4</sup>It should be noted that the frequency control action  $P_{fcr}$  and the grid frequency  $f$  are not denoted with subscript  $t$  because they are not controlled variables in the optimization problem. Instead,  $f$  depends on the interconnected power grid and  $P_{fcr}$  is the automatic response of GFM control with response time in the order of tens of milliseconds.

Similarly, for the reactive power:

$$Q_{set,t} = \sigma_v \cdot (v_{nom} - v_{ref,t}) \quad (3.24)$$

where  $v_{nom}$  is the nominal voltage. Equations (3.23) to (3.24) represent the relation between active and reactive power with frequency and voltage set-point fed to a GFM converter.

### 3.2.3.3. Real-time problem formulation

Finally, given a set-point in power  $P_{set,t}, Q_{set,t}$  (in order to prioritize the active power, the reactive power set-point  $Q_{set,t}$  can be set as zero) coming from the MPC problem, the GFM converter optimal references are computed by solving the following optimization problem:

$$\begin{aligned} [f_{ref,t}^*, v_{ref,t}^*] = \\ = \arg \min \lambda_P (P_{set}^* - P_{set,t})^2 + \lambda_Q (Q_{set}^* - Q_{set,t})^2 \end{aligned} \quad (3.25)$$

subject to (3.16) - (3.24), where (3.16) - (3.21) represent the relation between active/reactive power with the converter capability curve and (3.23), (3.24) represent the relation between active/reactive power with frequency/voltage set-point fed to the GFM controller. A way to convexify the problem in (3.25) subject to (3.16) - (3.21) has been presented in [24], while constraints (3.23) - (3.24) are linear, since  $\sigma_f$  and  $\sigma_v$  are fixed. The optimization problem is defined to find the optimal active and reactive power set-point compatibly with the capability curve of the converter. In particular, if the original set-points are feasible, the optimization problem returns the obvious solution  $P_{set}^* = P_{set,t}$  and the converter reference points are:

$$f_{ref}^* = f_{nom} - \frac{P_{set}^*}{\sigma_f} \quad (3.26)$$

$$v_{ref}^* = v_{nom} - \frac{Q_{set}^*}{\sigma_v} \quad (3.27)$$

## 3.3. Experimental validation

### 3.3.1. Experimental Setup

For the experimental campaign, a 20 kV distribution feeder in the EPFL campus equipped with a BESS is considered (see in Fig. 3.2). The distribution feeder includes a group of buildings characterised by a 140 kW base load, hosting 105 kWp roof-top PV installation and a grid-connected 720 kVA/500 kWh Lithium Titanate BESS. The targeted grid has a radial topology and is characterized by co-axial cables lines with a cross section of 95 mm<sup>2</sup> and a length of few hundreds meters, therefore, the grid losses are negligible [26]. The measuring systems is composed by a Phasor Measurement Unit (PMU)-based distributed sensing infrastructure. The measuring infrastructure allows for acquiring in real time accurate information of the power flows  $G$ ,  $L$  and  $P$ , thanks to the PMUs' fast reporting rate (i.e., 50 frame per second) and high accuracy which in terms of 1 standard deviation is equal to 0.001 degrees (i.e. 18  $\mu$ rad) [27].

### 3.3.2. Experimental Validation

This subsection reports the results of a day-long experiment, taking place on the EPFL campus on a working day (Friday, i.e., day-category C according to Appendix A).

### 3.3.2.1. Day ahead

The input and output information of the day-ahead dispatch process for the experimental day are shown in Fig. 3.4. The  $S = 10$  generated scenarios  $C$  for the prosumption are shown in Fig. 3.4a, where  $C^\downarrow$  and  $C^\uparrow$  are the lower and upper bounds shown in thick black lines, while all the scenarios are represented by thin colored lines. The upper and lower bound of the PV forecast, expressed in terms of PV production in kW, are shown in Fig. 3.4b, while the net demand scenarios at the PCC, obtained according to Eqs. (A.3) and (A.4), are shown in Fig. 3.4c. The upper and lower bound of the prosumption, namely  $L_n^\uparrow$  and  $L_n^\downarrow$ , are inputs to the dispatch plan. Finally, Fig. 3.4d and 3.4e show respectively the power and energy budget allocated for the forecasting uncertainty of the stochastic PV production (in dark gray) and demand (in light gray). The remaining energy budget is allocated for the FCR service, resulting in a droop  $\sigma_f = 116$  kW/Hz.

### 3.3.2.2. Dispatch tracking and primary frequency regulation

The results of the dispatch tracking are shown in Fig. 3.5. In particular, Fig. 3.5a shows the power at the PCC (in shaded gray), the prosumption (in dashed red) and the dispatch plan (in black). First, it is observed that the dispatch plan is tracked by the GFM-converter-interfaced BESS injecting active power (i.e., the shaded red area) to compensate for the mismatch between the prosumption and the dispatch plan. Second, when the grid-frequency has a significant deviation from 50 Hz, the GFM converter provides a non-negligible amount of power  $\Delta G^F$  to the feeder as a result of the frequency regulation. For instance, as shown in Fig. 3.5b, a considerable frequency is observed at the beginning of hour 10. Correspondingly, a non-negligible amount of active power for frequency regulation is injected by the BESS (see the shaded blue area in Fig. 3.5a). It is also observed that the contribution of primary frequency regulation causes a deviation of the average PCC power (the shaded gray area in 3.5a) from the dispatch plan (the black curve in 3.5a), as targeted by Eq. (3.9). Moreover, as visible in Fig. 3.5c the BESS SOC is contained within its physical limits over the day.

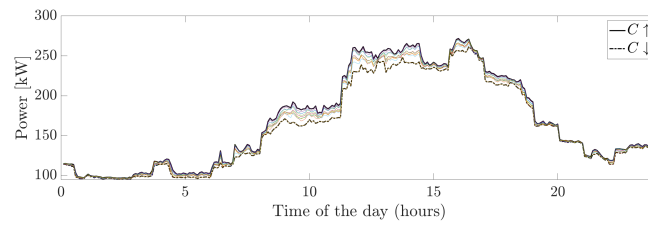
**Table 3.1:** Tracking error statistics (in kW)

	ME	MAE	RMSE
No Dispatch Tracking	-3.49	47.00	18.26
Dispatch Tracking	0.11	16.93	3.00
Dispatch + FCR Tracking	-0.45	0.79	1.43

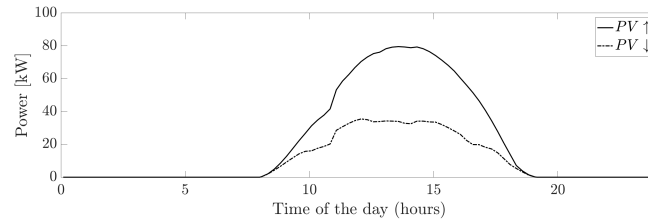
To evaluate the dispatch plan-tracking performance, *Root Mean Square Error* (RMSE), *Mean Error* (ME), and *Maximum Absolute Error* (MAE) are considered. In particular these indicators are visible in Table 3.1 for three different cases:

- (i) no dispatch case, where the error is computed as difference between prosumption and dispatch plan;
- (ii) dispatch tracking case, where the error is computed as difference between flow at the PCC and dispatch plan;
- (iii) dispatch tracking + FCR case, where the error is computed as difference between flow at the PCC and dispatch plan + FCR contribution, as targeted by the MPC problem (3.12a).

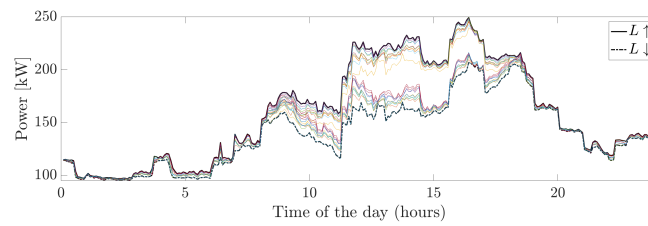
The obtained results are proving the good performance of the dispatch + FCR tracking framework. The overall results are comparable with the one presented in [5]. In this respect, operating BESSs as GFM units does not prevent them from achieving services that are expected in grid-following units.



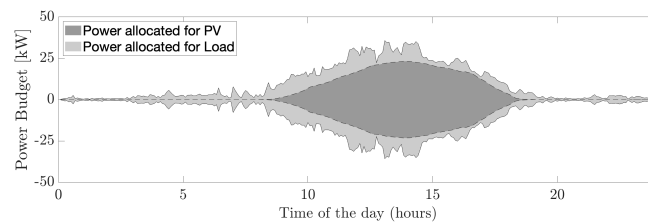
(a) Day-ahead load scenarios



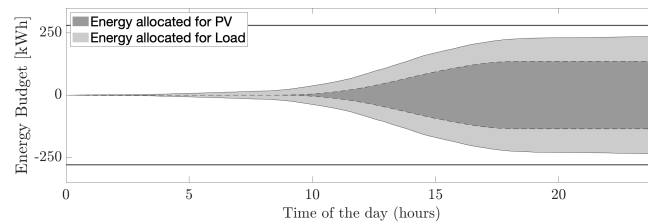
(b) Day-ahead PV forecast



(c) Day-ahead net demand scenarios



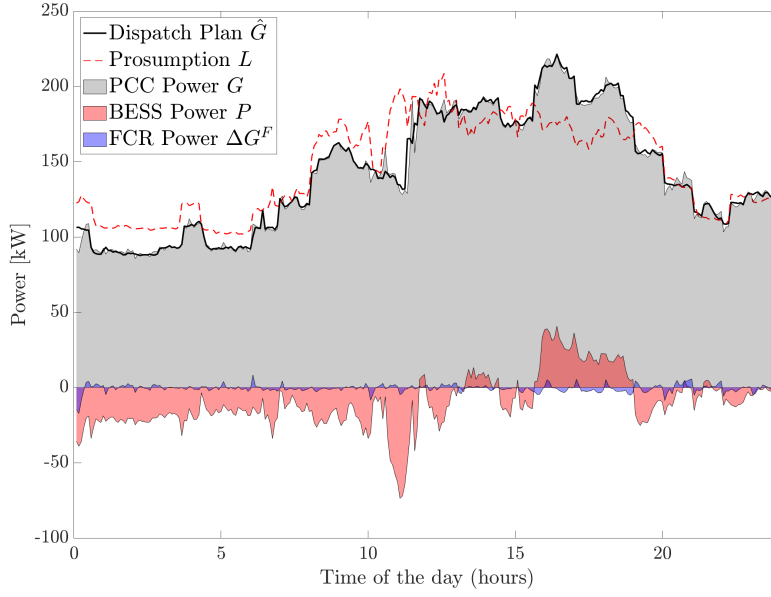
(d) BESS power budget



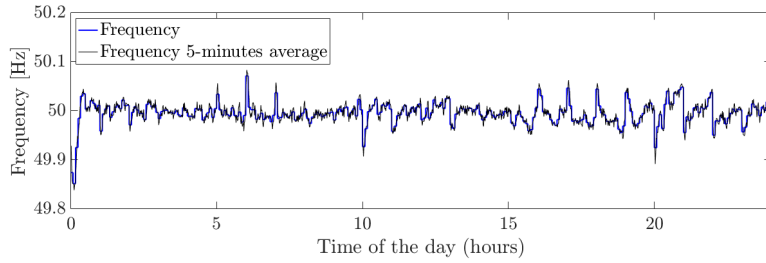
(e) BESS energy budget

**Figure 3.4:** Input and output of the day-ahead problem. (a) shows 10 demand generated scenarios, and their relative upper and lower bound. (b) shows the upper and lower bound for the PV production. (c) combines load and PV to show the prosumption scenario, input of the day ahead problem. (d) and (e) show the power and energy budget allocated to perform the different services.

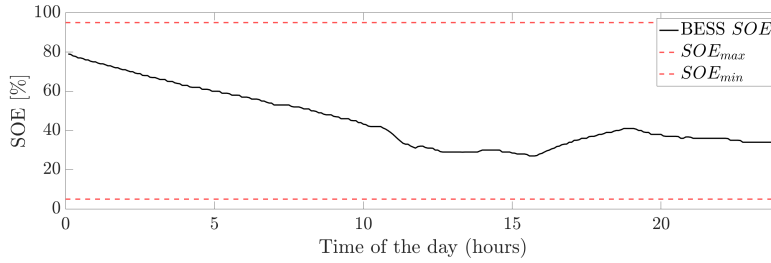
The day-ahead optimization problem and the MPC for dispatching tracking at intra-day stage are not affected by whether operating the BESS in GFM or GFL mode. As a result, the GFM mode has no impact on the remunerated services performed in the first two stages.



(a)



(b)



(c)

**Figure 3.5:** Experimental results for the 24-hour test. (a) compares the dispatch plan (in black) with: the measured power at the PCC (shaded gray), the prosumption of the feeder (in dashed red), the BESS power flow (in shaded red) and the average power required for each 5-minutes window for the provision of FCR service by the BESS. (b) shows the grid-frequency and its 5-minutes mean. The SOE of the battery during the test is visible in (c).

### 3.3.2.3. Short-term and local frequency regulation

To assess the performance of the GFM converter in regulating the frequency at the PCC, we adopt the metric named relative Rate-of-Change-of-Frequency (rRoCoF) proposed in [28], and defined as:

$$rRoCoF = \left| \frac{\Delta f_{PCC}/\Delta t}{\Delta P} \right| \quad (3.28)$$

where  $\Delta f_{PCC}$  is the difference between one grid-frequency sample and the next (once-differentiated value) at the PCC,  $\Delta P$  is the once-differentiated BESS active power, and  $\Delta t$  (i.e., 60 ms) is the sampling interval. As the metric rRoCoF is weighted by the delivered active power of the BESS, it can also be used to compare the effectiveness of converter controls (i.e., GFM vs GFL) in regulating frequency at local level in a large inter-connected power system. The grid-frequency is measured by a PMU installed at the PCC.

The rRoCoF is computed from different frequency timeseries, corresponding to the following four cases.

- *Case 1*: rRoCoF computed considering the 24 hour-long experiment where GFM-controlled BESS is providing multiple services.
- *Case 2*: rRoCoF computed considering a 15-minute window around a significant frequency transient (i.e., around 00:00 CET) during the same day-long experiment.
- *Case 3*: rRoCoF computed with a dedicated 15-minute experiment where GFM-controlled BESS is only providing FCR with its highest possible frequency-droop (1440 kW/Hz) during a significant grid-frequency transient.
- *Case 4*: rRoCoF computed with a dedicated 15-minute experiment where GFL-controlled BESS is only providing FCR with its highest possible frequency-droop (1440 kW/Hz) during a significant grid-frequency transient.

While *Case 1* and *Case 2* rely on the measurements obtained from the experiment carried out in this study, *Case 3* and *Case 4* leverage an historical frequency data-set, also used in the experimental validation proposed in [28]. It should be noted that the same experimental setup described in Section 3.3.1 is utilized in [28]. The measurements at hour transition are considered in order to evaluate GFM/GFL units' frequency regulation performance under relatively large frequency variations.

Fig. 3.6 shows the *Cumulative Density Function* (CDF) of the rRoCoF values for the four cases. First, it can be noted that, as expected, the CDF results of *Case 1* and *Case 2* are very close. In particular since rRoCoF is normalised by the BESS power injection, the frequency dynamic and the frequency droop of the BESS controller have little effect on the result of CDF. Moreover, the comparison between *Case 2* and *Case 3* shows negligible differences on the rRoCoF CDF, proving that the provision of dispatchability service by the GFM converter does not affect its frequency regulation performance. Finally, the comparison between GFM and GFL-controlled BESS (i.e., *Case 2* vs *Case 4*) is reported from [28], to show that GFM unit achieves significantly lower rRoCoF for per watt of regulating power injected by the BESS.

To conclude, a comprehensive framework for the simultaneous provision of multiple services (i.e. feeder dispatchability, frequency and voltage regulation) to the grid by means of a GFM-converter-interfaced BESS has been proposed. The framework consists of three stages. The day-ahead stage determines an optimal dispatch plan and a maximum frequency droop coefficient by solving a robust optimization problem that accounts for the uncertainty of forecasted presumption. In the intra-day stage, a MPC method is used in the operation process to achieve the tracking of dispatch plan while allowing for frequency containment reserve properly delivered by the BESS. Finally, the real-time controller is implemented to convert the power set-points from MPC into frequency references accounting for the PQ feasible region of the converter.

The experimental campaign carried out in a 20 kV distribution feeder in the EPFL campus. The feeder includes a group of buildings characterised by a 140 kW base load, hosting 105 kWp roof-top PV installation and a grid-connected 720 kVA/500 kWh Lithium Titanate BESS. A 24-hour long experiment proved good performance in terms of dispatch tracking, compatible with the ones obtained in [5] for sole provision of dispatchability by means of GFL converter-interfaced BESS. Moreover, the rRoCoF metric has been used to show that the provision of dispatchability service by the GFM converter does not affect its frequency regulation performance and confirm the positive effects of GFM con-

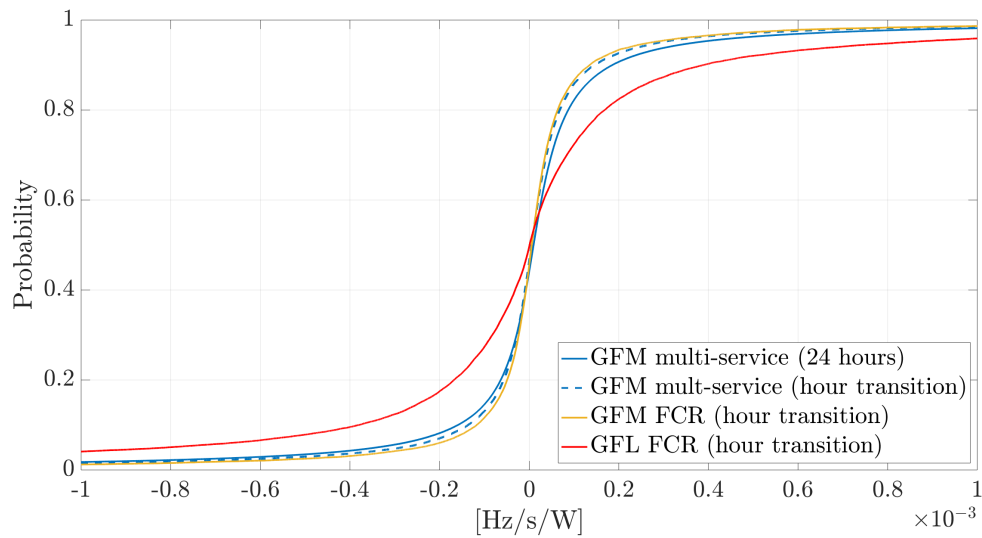


**Figure 3.6:** Cumulative Density Function of rRoCoF.

verters with respect to the GFL ones in the control of the local frequency. Future works concern the development of control strategies to prioritize the FCR service when the battery is operating close to its operational limit, as required by grid-codes. Moreover, an analysis on the effects of voltage regulation on the BESS losses could be included in the day ahead scheduling problem.

## 4. Conclusions

This deliverable assessed the performance of the two multi-service control algorithms specifically designed for BESSs. The performance of both frameworks have been validated at EPFL leveraging a utility-scale 720 kVA/560 kWh BESS connected to a medium feeder radial feeder of the EPFL campus medium voltage grid.

The first part presented and validates a BESS control framework for the optimal provision of concurrent primary frequency and local voltage control, achieved via the modulation of active and reactive power set-points respectively, exploiting the flexibility given by the four-quadrant power converter. The proposed algorithm considers the working conditions of the AC utility grid as well as the battery DC voltage as a function of the current trajectory using the battery TTC model. This allows for the selection of the suitable converter capability curve, which is not unique for all the possible BESS operating conditions, hence optimizing the provision of grid services. A computationally-efficient algorithm was proposed to solve the formulated optimal power set-points calculation problem. The experimental campaign showed the controller's capability to enable FCR and local voltage control. In case of large initial droop constants or large frequency/voltage deviations, the PQ feasible region is binding and the proposed controller enabled the operation at the edge of the selected PQ capability curve, dramatically reducing the amount of accumulated non-delivered regulating power during the control session. Hence, this work highlights the importance of accurately modelling the employed hardware in order to enable an optimal grid service provision even under non-nominal BESS conditions (e.g., reduced the available number of strings) as well as under commercial hardware embedded technical limitations (e.g., variable capability curves of the power converter).

The second part proposes and validates a comprehensive framework for the simultaneous provision of multiple services to the grid by means of a GFM-converter-interfaced BESS. The framework consists of three stages. The day-ahead stage determines an optimal dispatch plan and a frequency (and voltage) droop coefficient by solving a robust optimization problem that accounts for the uncertainty of forecasted prosumption. In the intra-day stage, a MPC method is used in the operation process to achieve the tracking of dispatch plan while allowing the provision of frequency containment reserve by the BESS. Finally, the real-time controller is implemented to convert the power set-points from MPC into frequency references accounting for the PQ feasible region of the converter. The experimental campaign was carried out in a 20 kV distribution feeder in the EPFL campus. The feeder includes a group of buildings characterised by a 140 kW base load, hosting 105 kWp roof-top PV installation and a grid-connected 720 kVA/500 kWh Lithium Titanate BESS. A 24-hour long experiment proved good performance in terms of dispatch tracking, demonstrating that operating BESSs as GFM units does not prevent them from achieving services that are expected in grid-following units. In addition, since the day-ahead and the MPC dispatching tracking stages are not affected by whether operating the BESS in GFM or GFL mode, the remunerated services performed at the first two stages are not affected by the converter control mode. On the other hand, the rRoCoF metric is used to show that the provision of dispatchability service by the GFM converter does not affect its frequency regulation performance and confirms the positive effects of grid-forming converters with respect to the grid-following ones in the control of the local frequency.

## Bibliography

- [1] E. Rehman, M. Miller, J. Schmall, and S. Huang, “Dynamic stability assessment of high penetration of renewable generation in the ERCOT grid,” ERCOT, Austin, Tx, Tech. Rep., 2018.
- [2] AEMO, “Maintaining power system security with high penetrations of wind and solar generation,” 2019.
- [3] F. Conte, S. Massucco, G.-P. Schiapparelli, and F. Silvestro, “Day-ahead and intra-day planning of integrated bess-pv systems providing frequency regulation,” *IEEE Transactions on Sustainable Energy*, vol. 11, no. 3, pp. 1797–1806, 2020.
- [4] E. Namor, F. Sossan, R. Cherkaoui, and M. Paolone, “Control of battery storage systems for the simultaneous provision of multiple services,” *IEEE Transactions on Smart Grid*, vol. 10, no. 3, pp. 2799–2808, May 2019.
- [5] F. Sossan, E. Namor, R. Cherkaoui, and M. Paolone, “Achieving the dispatchability of distribution feeders through prosumers data driven forecasting and model predictive control of electrochemical storage,” *IEEE Transaction on Sustainable Energy*, vol. 7, no. 4, pp. 1762–1777, Oct 2016.
- [6] J. Wang, S. Hashemi, S. You, and C. Trøeholt, “Active and reactive power support of mv distribution systems using battery energy storage,” in *2017 IEEE International Conference on Industrial Technology (ICIT)*, 2017, pp. 382–387.
- [7] E. Serban, M. Ordonez, and C. Pondiche, “Voltage and frequency grid support strategies beyond standards,” *IEEE Transactions on Power Electronics*, vol. 32, no. 1, pp. 298–309, 2017.
- [8] Y. Zuo, Z. Yuan, F. Sossan, A. Zecchino, R. Cherkaoui, and M. Paolone, “Performance assessment of grid-forming and grid-following converter-interfaced battery energy storage systems on frequency regulation in low-inertia power grids,” *Sustainable Energy, Grids and Networks*, Sep. 2021.
- [9] Y. Zuo, M. Paolone, and F. Sossan, “Effect of voltage source converters with electrochemical storage systems on dynamics of reduced-inertia bulk power grids,” *Electric Power Systems Research*, vol. 189, p. 106766, Dec. 2020.
- [10] J. Liu, Y. Miura, and T. Ise, “Comparison of Dynamic Characteristics Between Virtual Synchronous Generator and Droop Control in Inverter-Based Distributed Generators,” *IEEE Transactions on Power Electronics*, vol. 31, no. 5, pp. 3600–3611, May 2016. [Online]. Available: <http://ieeexplore.ieee.org/document/7182342/>
- [11] T. Qoria, E. Rokrok, A. Bruyere, B. Francois, and X. Guillaud, “A PLL-Free Grid-Forming Control With Decoupled Functionalities for High-Power Transmission System Applications,” *IEEE Access*, vol. 8, pp. 197 363–197 378, 2020. [Online]. Available: <https://ieeexplore.ieee.org/document/9240975/>
- [12] R. Rosso, S. Engelken, and M. Liserre, “Robust Stability Analysis of Synchronverters Operating in Parallel,” *IEEE Transactions on Power Electronics*, vol. 34, no. 11, pp. 11 309–11 319, Nov. 2019. [Online]. Available: <https://ieeexplore.ieee.org/document/8630646/>
- [13] M. Z. Lazkano, J. J. Valera, C. Cardozo, T. Prevost, G. Denis, Y. Vernay, Y. Zuo, A. Zecchino, Z. Yuan, R. Cherkaoui, and M. Paolone, “Deliverable 3.3: Analysis of the synchronisation capabilities of bess power converters.”
- [14] F. Sossan, E. Namor, R. Cherkaoui, and M. Paolone, “Achieving the dispatchability of distribution feeders through prosumers data driven forecasting and model predictive control of electrochemical storage,” *IEEE Transactions on Sustainable Energy*, vol. 7, no. 4, pp. 1762–1777, Oct 2016.
- [15] E. Namor, “Advanced models and algorithms to provide multiple grid services with

- 
- battery storage systems.” Lausanne: EPFL, 2018, p. 196. [Online]. Available: <http://infoscience.epfl.ch/record/256959>
- [16] E. Namor, F. Sossan, E. Scolari, R. Cherkaoui, and M. Paolone, “Experimental assessment of the prediction performance of dynamic equivalent circuit models of grid-connected battery energy storage systems,” in *2018 IEEE PES Innovative Smart Grid Technologies Conference Europe (ISGT-Europe)*, Oct 2018, pp. 1–6.
- [17] M. Pignati, M. Popovic, S. Barreto, R. Cherkaoui, G. Dario Flores, J. Le Boudec, M. Mohiuddin, M. Paolone, P. Romano, S. Sarri, T. Tesfay, D. Tomozei, and L. Zanni, “Real-time state estimation of the epfl-campus medium-voltage grid by using pmus,” in *2015 IEEE Power Energy Society Innovative Smart Grid Technologies Conference (ISGT)*, 2015, pp. 1–5.
- [18] “Swiss technical standard - framework agreement for the supply of primary control power,” 2016.
- [19] “Danish technical standard - technical regulation 3.3.1 for electrical energy storage facilities,” 2019. [Online]. Available: <https://en.energinet.dk/Electricity/Rules-and-Regulations/Regulations-for-grid-connection>
- [20] AEMC, “Review of the system black event in south australia on 28 september 2016,” Technical Report - 2019. [Online]. Available: [https://www.aemc.gov.au/sites/default/files/documents/aemc\\_-\\_sa\\_black\\_system\\_review\\_-\\_final\\_report.pdf](https://www.aemc.gov.au/sites/default/files/documents/aemc_-_sa_black_system_review_-_final_report.pdf)
- [21] S. Lu, P. V. Etingov, D. Meng, X. Guo, C. Jin, and N. A. Samaan, “Nv energy large-scale photovoltaic integration study: Intra-hour dispatch and agc simulation,” Pacific Northwest National Lab.(PNNL), Richland, WA (United States), Tech. Rep., 2013.
- [22] G. du Réseau de Transport d’Electricité (RTE), “Frequency Ancillary Services Terms and Conditions,” May 2020.
- [23] “COMMISSION REGULATION (EU) 2016/ 631 - of 14 April 2016 - establishing a network code on requirements for grid connection of generators,” p. 68.
- [24] A. Zecchino, Z. Yuan, F. Sossan, R. Cherkaoui, and M. Paolone, “Optimal provision of concurrent primary frequency and local voltage control from a bess considering variable capability curves: Modelling and experimental assessment,” *Electric Power Systems Research*, vol. 190, p. 106643, 2021.
- [25] E. Scolari, L. Reyes-Chamorro, F. Sossan, and M. Paolone, “A comprehensive assessment of the short-term uncertainty of grid-connected pv systems,” *IEEE Transactions on Sustainable Energy*, vol. 9, no. 3, pp. 1458–1467, 2018.
- [26] Marco Pignati et al., “Real-time state estimation of the EPFL-campus medium-voltage grid by using PMUs,” in *2015 IEEE Power & Energy Society Innovative Smart Grid Technologies Conference (ISGT)*. Washington, DC, USA: IEEE, Feb. 2015, pp. 1–5.
- [27] L. Zanni, A. Derviškić, M. Pignati, C. Xu, P. Romano, R. Cherkaoui, A. Abur, and M. Paolone, “Pmu-based linear state estimation of lausanne subtransmission network: Experimental validation,” in *21st PSCC*, July 2020.
- [28] A. Zecchino et al., (in press), “Local Effects of Grid-Forming Converters Providing Frequency Regulation to Bulk Power Grids,” in *2021 IEEE PES Innovative Smart Grid Technology – Asia*. IEEE, Dec. 2021, p. 5.
- [29] B.-J. Chen, M.-W. Chang, and C.-J. Lin, “Load Forecasting Using Support Vector Machines: A Study on EUNITE Competition 2001,” *IEEE Transactions on Power Systems*, vol. 19, no. 4, pp. 1821–1830, Nov. 2004.
- [30] F. Sossan, E. Scolari, R. Gupta, and M. Paolone, “Solar irradiance estimations for modeling the variability of photovoltaic generation and assessing violations of grid constraints: A comparison between satellite and pyranometers measurements with load flow simulations,” *Journal of Renewable and Sustainable Energy*, vol. 11, no. 5, p. 056103, Sep. 2019.

- 
- [31] F. Pozzi, T. Di Matteo, and T. Aste, "Exponential smoothing weighted correlations," *The European Physical Journal B*, vol. 85, no. 6, p. 175, Jun. 2012.
- [32] G. Piero Schiapparelli, S. Massucco, E. Namor, F. Sossan, R. Cherkaoui, and M. Paolone, "Quantification of Primary Frequency Control Provision from Battery Energy Storage Systems Connected to Active Distribution Networks," in *2018 Power Systems Computation Conference (PSCC)*. Dublin: IEEE, Jun. 2018, pp. 1–7.

## A. Forecasting Tools

Once the optimization problem Eqs. (3.4a) to (3.4e) is defined, an important challenge stands in the forecast of the prosumption and the frequency deviation, in particular their confidence intervals, denoting the maximum and minimum expected realisations, namely  $L_n^\uparrow$ ,  $L_n^\downarrow$  and  $W_{f,k}^\uparrow$ ,  $W_{f,k}^\downarrow$ . As correctly stated in [5], the local prosumption is characterized by a high volatility due to the reduced spatial smoothing effect of PV generation and the prominence of isolated stochastic events, such as induction motors intrusions due to the insertion of pumps or elevators. For these reasons, the existing forecasting methodologies, developed by considering high levels of aggregation, e.g. [29], are not suitable to predict low populated aggregates of prosumers. For the proposed application, the problem of identifying  $L_n^\uparrow$  and  $L_n^\downarrow$  is divided into two sub-problems: (i) load consumption forecast and (ii) PV production forecast.

For the first one, a simple non-parametric forecasting strategy relying on the statistical properties of the time series is proposed. The PV production forecast is performed by taking advantage of solar radiation and meteorological data services providing a day-ahead prediction of the *Global Horizontal Irradiance* (GHI) together with its uncertainty. The GHI forecast, together with the information related to the PV installation (i.e. total capacity, location, tilt, azimuth) allows computing the *Global Normal Irradiance* (GNI) and obtaining an estimation of the total PV production, and the related uncertainties. The best and worst PV production scenarios are computed by transposing the GHI forecast data and applying a physical model of PV generation accounting for the air temperature [30]. For a given day-ahead forecast, the vector containing the best and worst production scenario for the PV, with a time resolution of 5 minute are named as  $PV^\uparrow$  and  $PV^\downarrow$ , respectively.

As previously mentioned, while the PV production forecast leverages GHI data, the load forecast only relies on statistical properties of recorded time-series. In particular, a set of historical observation  $\mathcal{G}$  at the PCC point is considered. The historical load consumption  $\mathcal{C}$  is computed for every time step  $n$  corresponding to a 5 minutes window and every day  $d$ , as:

$$\begin{aligned} \mathcal{C}_{n,d} &= \mathcal{G}_{n,d} - \mathcal{P}_{n,d} - \mathcal{PV}_{n,d} \\ \forall n \in [1, N] \quad \forall d \in [1, D] \end{aligned} \quad (\text{A.1})$$

where  $\mathcal{P}_n$  is the historical measure of the BESS power at time  $n$  and  $\mathcal{PV}_n$  is the estimated PV production at the same time relying on the onsite measures of GHI, and  $D$  is the total number of recorded days. The process described by Eq. (A.1), also known as disaggregation, allows for the decoupling of the PV production and the load consumption  $\mathcal{C}$ , composed by 288 samples for each recorded day. The different consumption scenarios are generated by applying the following heuristic.

- The data-set  $\mathcal{C}$  is divided into sub-sets  $\Omega_{A,B,C,D1,D2}$  by selecting consumption data corresponding respectively to: (A) first working day of the week, i.e. Mondays or days after holidays; (B) central working days of the week, i.e. Tuesdays, Wednesdays and Thursdays; (C) last working day of the week, i.e. Friday or days before holidays; (D) holidays, i.e. Saturday (sub-category D1), Sundays and festivities (subcategory D2).
- For each sub-set, the statistical properties  $\mu$  and  $\sigma$  are inferred as:

$$\begin{aligned} \mu_\Omega &= \text{mean}(\Omega) \quad \sigma_\Omega = \text{cov}(\Omega) \\ \forall \Omega \in [\Omega_{A,B,C,D1,D2}] \end{aligned} \quad (\text{A.2})$$

where the function `mean` returns an array of 288 points, each of which represents a mean value for a particular 5-minutes window of the day and the function `cov` returns a 288x288 matrix corresponding to the covariance matrix of the observation.

- Both  $\mu_\Omega$  and  $\sigma_\Omega$  are computed by considering an exponential forgetting factor to prioritise the

---

latest measurement with respect to the older one, as defined in [31].

- A given number  $S$  of possible scenarios is generated by considering the same multivariate normal distribution, with mean equal to  $\mu$  and covariance equal to  $\sigma$
- $C^\downarrow$  and  $C^\uparrow$  are defined as the load scenarios characterised by the lowest and highest load profile, respectively.

Finally, the presumption minimum end maximum expected realisation are computed by combining  $C^\downarrow$  and  $C^\uparrow$  with  $PV^\uparrow$  and  $PV^\downarrow$  as follows:

$$L_n^\uparrow = C_n^\uparrow - PV_n^\downarrow \quad (\text{A.3})$$

$$L_n^\downarrow = C_n^\downarrow - PV_n^\uparrow \quad (\text{A.4})$$

$$\forall n \in [1, N]$$

Concerning the prediction of  $W_f$ , while [4] only relies on the statistical properties of the time series, this paper uses an auto regressive model, as supported by [32] which indicates the possibility to predict  $W_f$  to reduce the variance of the forecast in respect to the historical variance of the time series.